CARBON DIOXIDE HYDROGENATION TO METHANOL OVER $Cu/ZnO/ZrO_2$/EAGS CATALYSTS

by

Amir Seidshazileh

Submitted in partial fulfilment of the requirements
for the degree of Master of Applied Sciences

at

Dalhousie University
Halifax, Nova Scotia
December 2023

Dalhousie University is located in Mi'kma'ki, the
ancestral and unceded territory of the Mi'kmaq.
We are all Treaty people.

Table of Contents

LIST OF TABLES

LIST OF FIGURES

ABSTRACT

The rapidly increasing carbon dioxide (CO_2) emissions caused a substantial negative impact on the environment. It led to environmental problems, such as global warming, ocean acidification and climate change. To mitigate CO_2 emissions, carbon capture and utilization make more sense than carbon storage. CO_2 hydrogenation to methanol is a promising process for converting renewable energy into valuable fuels and chemicals, which can combat the emissions of greenhouse gases associated with using fossil resources. Catalytic conversion plays key role in the efforts to convert CO_2 into methanol, not only technically but also economically. The significant challenge remains to achieve a highly active, selective, and stable catalyst acceptable in industrial processes. While $Cu/ZnO/ZrO_2$ is a promising catalyst for unleashing methanol production, its industrial potential remains unfulfilled due to insufficient performance and stability. Consequently, EAGs have been introduced as an additive to bolster the catalyst's effectiveness. The objective of this research is to develop and characterize a Cu/ZnO/ZrO2 catalyst incorporated with EAG to investigate the impact of EAG addition on catalyst performance. The synthesis involved the preparation of catalysts with EAGs through the co-precipitation method, followed by comprehensive characterization using XRD, SEM, N_2 physisorption, H_2-TPR, and CO_2-TPD techniques.

The findings suggest that the controlled addition of a small quantity of EAGs led to a notable reduction in the size of Cu particles, creating more catalytically active Cu sites on the catalyst's surface for CO/CO_2 hydrogenation reactions and increasing the specific surface area. Conversely, a higher EAG content may cause a reduction in specific surface area of the active part of the catalyst. SEM observations support these conclusions, revealing increased irregularity in particle shapes and larger particle sizes at higher EAG concentrations. Furthermore, the introduction of a small quantity of EAGs notably improved hydrogen absorption. The most impressive enhancement was a 1.47-fold increase in absorption at lower temperatures, coupled with a remarkable 1.6-fold overall increase in absorption compared to catalysts without EAGs. This enhancement is attributed to the EAGs' capacity to act as effective adsorbents, activators, and reservoirs for H_2. This, in turn, facilitates the creation of microenvironments with a higher, steady-state concentration of active hydrogen on the catalyst's surface, thereby promoting the efficiency of CO/CO_2 hydrogenation reactions. In addition, CO_2-TPD profiles reveal that the addition of EAGs promotes the total CO_2 desorption by 1.21-fold and elevates temperature peaks, favouring more selective methanol production. Fixed-bed plug flow reactor has been designed, and parts have been ordered to investigate the activity of the catalyst.

LIST OF ABBREVIATIONS USED

CO_2	Carbon dioxide
CH_4	Methane
CH_3OH	Methanol
N_2O	Nitrous oxide
SF_6	Sulphur hexafluoride
In_2O_3	Indium oxide
HNO_3	Nitric acid
$CuN_2O_6.\ 3H_20$	Copper (II) nitrate trihydrate
$N_2O_6Zn.\ 6H_2O$	Zinc nitrate hexahydrate
$N_2O_7Zr.\ xH_2O$	Zirconium (IV) oxynitrate hydrate
Na_2CO_3	Sodium carbonate
CCZ	$Cu/ZnO/ZrO_2$
GO	Graphene oxide
r-GO	Reduced graphene oxide
IPCC	International Panel of Climate Change
CCS	CO_2 capture and storage
CCU	CO_2 capture and utilization
EOR	Enhanced oil recovery
IUPAC	International Union of Pure and Applied Chemistry
ICI	Imperial Chemical Industries
CRI	Carbon Recycling International
COG	Coke oven gas production
RWGS	Reverse Water Gas Shift
TOF	Turnover frequency
DFT	Density functional theory
ER	Eley-Rideal
TGI	Template genetic inheritance

MOF	Metal-organic framework
BET	Brunauer, Emmet, and Teller
XRD	X-ray diffraction
ICDD	International Centre for Diffraction Data
NLDF	Nonlocal density functional
PSD	Pore size distribution
SEM	Scanning electron microscope
EDX	Energy Dispersive X-ray
ICP-MS	Inductively Coupled Plasma Mass Spectrometry
M/Z	Mass-to-charge ratio
TPR	Temperature-programmed reduction
H_2-TPR	H_2 temperature-programmed reduction
TPD	Temperature-programmed desorption
CO_2-TPD	CO_2 Temperature-programmed desorption
TCD	Thermal conductivity detector
PID	Proportional integral derivative
GC	Gas chromatograph
FID	Flame ionization detector
NIST	National Institute of Standards and Technology
PDF	Pair distribution function analysis
GHSV	Gas Hourly Space Velocity
Ppm	Parts per million

ACKNOWLEDGEMENTS

I wish to express my profound gratitude to my supervisor, Dr. George Jarjoura, for his unwavering guidance and support throughout my master's program at Dalhousie University. I would also like to extend my appreciation to Dr. Zoheir Farhat and Dr. Hany Elnaggar for their valuable contributions as members of my supervisory committee. Furthermore, I appreciate Dr. Eric Moreau for his assistance, training, and expertise in conducting H_2-TPR and CO_2-TPD, which were integral to my research. Additionally, I would like to express my gratitude to Cat Adalay for her expertise and guidance in designing industrial products.

Finlay, I wish to acknowledge the invaluable support, tremendous patience, and constant care provided by my family throughout this research program.

Amir Seidshazileh

December 2023

CHAPTER 1 Introduction

1.1 Carbon dioxide: Current scenario

The consumption of energy worldwide is continuously growing due to the increase in population and economic development. Fossil fuels, such as coal, gas, and petroleum, are currently the primary energy source—their production results in two-thirds of the world's greenhouse gas emissions, mainly carbon dioxide (IEA, 2023). To combat climate change, there was an agreement in Paris on December 12, 2015, which aimed to restrict the increase in the global average temperature to below 2 °C compared to pre-industrial levels by the end of the century. Several countries have taken steps toward achieving the agreement's goals (UNFCCC, 2015).

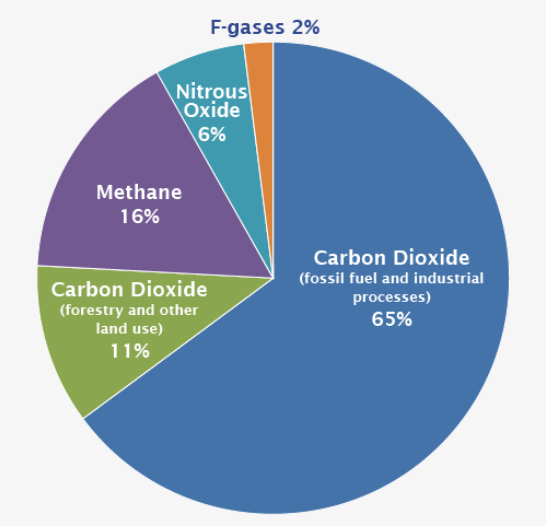

Figure 1.1: Global Greenhouse gas emission by gas (EPA, 2023).

1.1.1 CO_2 emission and the impact on lifestyle

According to the (IEA, 2023), there has been a continuous increase in carbon dioxide emissions worldwide since the pre-industrial era, with a recorded amount of 36.8 Bt in 2022. The primary energy supply worldwide has also risen by over 150% from 1971 to 2019, primarily due to the increasing demand for energy to support economic growth and development.

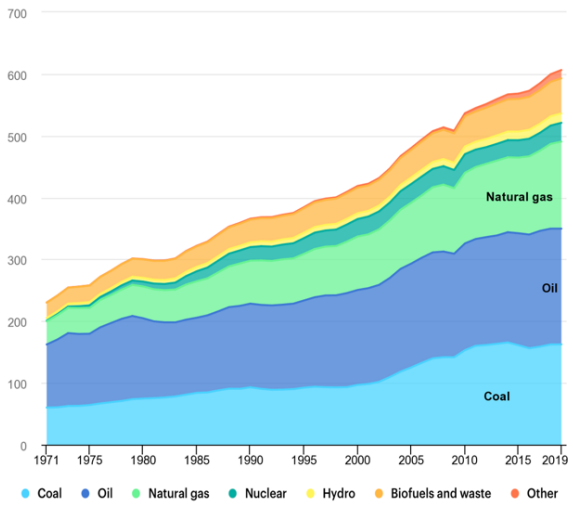

Figure 1.2: World total energy supply by source, 1971-2019 (IEA, 2023)

Although there have been significant advancements in renewable and nuclear energy sources over the past few decades, considered low or zero-carbon-emitting energy sources, fossil fuels still serve as the primary energy source worldwide. The use of fossil fuels for power generation is a significant contributor to carbon dioxide emissions. This trend is expected to continue in the coming years, as several countries, including Australia, China, India, Poland, and South Africa, generate more than two-thirds of their total electricity and heat by burning fossil fuels (EPA, 2023).

Before the late 17th century, the carbon dioxide concentration in the atmosphere was stable, and the natural carbon cycle was maintained. However, after the Industrial Revolution, the rate of human-caused CO_2 emissions gradually increased, resulting in a current concentration of 423 ppm. It took approximately 200 years for the first 50 ppm increase from the stable CO_2 concentration, while the subsequent 50 ppm increase occurred over 33 years (from 1973 to 2006). The remaining

43 ppm increase happened in the past 17 years. A summary of the changes in CO_2 concentration over the past 1000 years is provided in Table 1 (Global CO_2 levels, 2023).

Table 1.1: Variation of CO_2 concentration over the past 1000 years.

Year	Period (years)	Concentration (ppm)	Increase (ppm)	Increase rate (ppm year)
1000-1800	800	270-280	10	0.01
1800-1950	150	280-310	30	0.2
1958-1973	15	315-330	15	1
1973-2006	33	330-380	50	1.5
2006-2023	17	380-423	43	2.5

Initially, it may seem odd to consider CO_2 as a threat to plant and animal life. However, a sudden rise in CO_2 concentration, which is relatively rapid in the context of the Earth's extended climate history, can have an unfavourable impact on the climate and, thus, the ecosystem. Every year, about 120 Gt of CO_2 is released into the atmosphere through the natural carbon cycle, generated from living organisms' respiration and soil organic matter decomposition. It is assumed that a similar quantity of CO_2 is utilized through natural photosynthesis, which helps to sustain a relatively stable CO_2 concentration of around 280±10 ppm. However, the carbon cycle has been disrupted due to increased CO_2 concentration in the ocean and the change in land use. The ability of land and ocean to take up CO_2 is not enough to complete the carbon cycle, resulting in an accumulation of CO_2 from the anthropogenic emission and from the natural fluxes. Consequently, CO_2 remains in the atmosphere, leading to increased CO2 concentration and further global warming (EPA, 2023).

Svante Arrhenius first proposed the relationship between atmospheric CO_2 and the average global temperature in 1896, identifying CO_2 as a contributor to the greenhouse gas effect. The heat retained by greenhouse gases such as CO_2, CH_4, N_2O, and SF_6 from solar radiation has helped to maintain the Earth's temperature. However, an increase in heat-trapping gases, mainly CO_2, in the

atmosphere has led to a rise in the global temperature and subsequent global warming. The current level of atmospheric CO_2 is responsible for 9-26% of the natural greenhouse gas effect, making it the most critical climate regulator alongside water vapour, which mainly comes from the energy sector (Kiehl & Trenberth, 1997). Based on Arrhenius's model and recent studies, it's been estimated that there is a direct correlation between CO_2 concentration and temperature anomaly. If the current rate of CO_2 concentration increase continues, there will likely be a considerable temperature rise within the next century. The International Panel of Climate Change (IPCC), which monitors global climate change, has projected that a doubling of CO_2 concentration is likely to cause a rise in the global average temperature of between 2 and 4.5 °C. While long-term climate changes are difficult to predict, most scientists believe that events such as melting Arctic Ocean ice, glacier retreats, and rising sea levels are the result of this phenomenon. If the average global temperature were to increase by 2 °C, it would result in life-threatening consequences such as widespread droughts and extreme weather events. Dealing with the human-caused emissions of CO_2 and finding ways to utilize CO_2 are major challenges facing humanity (Brahic, 2007).

1.1.2 CO_2 mitigation strategies

The mitigation of carbon dioxide emissions and the prevention of catastrophic consequences resulting from climate change can be achieved through four pathways.

i. Improve technology in the power and industrial sectors to increase efficiency.
ii. Replace fossil fuel resources with renewable energy resources.
iii. Capture and store CO_2 through chemical or physical means (CCS).
iv. Use CO_2 to create chemicals and fuels (CCU).

The energy and chemical sectors have a significant opportunity for technical improvement to reduce CO_2 emissions and increase energy efficiency in the industry. For example, new natural gas and nuclear power plants could be used to achieve this goal. The use of renewable energy resources is still in the early stages, although research shows that it has the potential to replace

fossil fuel resources. However, it has yet to be ready for industrial applications. While options i) and ii) may be possible future scenarios for the energy and process sectors, they do not offer short or mid-term sustainable solutions. Therefore, finding an effective and reliable way to manage global CO_2 emissions is essential. The last two options (CCS and CCU) have the potential to control and reduce overall CO_2 levels to an acceptable degree (Gaikwad, 2018).

1.1.2.1 CO_2 capture and storage (CCS)

Over the past few decades, there have been ongoing improvements in CO_2 capture technology. The primary targets for implementing CO_2 capture technologies are power plants, fuel processing plants, and extensive industrial facilities such as those used for iron, steel, and cement production. Carbon capture and storage (CCS) refers to a set of technologies and techniques that capture CO_2 emissions and store them in geological formations, deep underground or under the ocean floor (Zapantis, et al., 2022). One example of carbon capture and storage (CCS) in Canada is the Boundary Dam Carbon Capture Project in Saskatchewan. This project captures CO_2 emissions from the flue gas of a coal-fired power plant and then stores the captured CO_2 in deep geological formations. The project has been in operation since 2014 and can capture up to one million tonnes of CO_2 annually. It is the first commercial-scale CCS project in the world to be applied to a coal-fired power plant, and it is expected to reduce greenhouse gas emissions by approximately one million tonnes per year (Zapantis, et al., 2022).

However, the CO_2 captured from large plants must be close to storage wells, to avoid energy-intensive transportation to the storage location. Another disadvantage of CCS is its high cost, which requires significant capital investment and operational expenses. Capturing, transporting, and storing CO_2 requires a lot of energy and infrastructure, which can be expensive to build and maintain. Additionally, CCS technologies still need to fully mature and their effectiveness in reducing CO_2 emissions and environmental impacts in the long term is still under evaluation. There are also concerns about the safety and long-term viability of storing large amounts of CO_2

underground or underwater, as it may pose potential risks of leakage and environmental damage (Gaikwad, 2018).

1.1.2.2 Capture and utilization (CCU)

In CCU, CO_2 is utilized as a chemical building block for creating valuable products rather than being stored. This approach complements CCS, achieving similar aims while providing economic advantages. CCU is a broad area of study that can be broadly divided into two main categories:

(A) Direct utilization of CO_2 based on its physical properties.

(B) Chemical applications that involve transforming CO_2 into a range of valuable chemicals and fuels.

The feasibility of using carbon dioxide depends mainly on the purity of the available CO_2. CO_2 obtained from certain fertilizers, natural gas processing, and cement production is typically considered a pure and clean source. Utilizing CO_2 captured from these pure and clean sources in an energy-efficient manner can reduce the global warming impact of many high-value economic processes (Minett, 2013).

Table 1.2: Major industrial processes which produce CO_2 (Minett, 2013)

Industry	**CO_2 produced ($Mt\ yr^{-1}$)**
Oil Refining	850-900
Cement Production	1000
Iron/Steel Production	870
Fermentation	200
Ammonia Synthesis	160
Ethene Synthesis	155
LNG Sweetening	20-25
Ethylene Oxide Synthesis	10

1.1.2.2.1 Direct use of CO_2

CO_2 alone, without any conversion or chemical transformation, has various applications such as food processing, preservation, beverage carbonation, coffee decaffeination, fire suppression, production of pharmaceuticals, and enhanced oil recovery. CO_2 injection in the beverage industry provides carbonation to water, cold drinks, beer, and dairy products, giving them a sparkling appearance, astringency, and refreshing taste. In the food industry, the modified atmosphere packaging technique increases the shelf life of fresh and chilled products such as meat, fish, fruits, and vegetables. Supercritical CO_2 under pressure extracts bitter flavours and decaffeinate coffee beans. CO_2 is also used as a fire suppressor by reducing oxygen concentration near the fire area and lowering the flame temperature and speed. The most practical method to make direct use of CO_2 is Enhanced oil recovery (EOR), the injection of CO_2 into depleted oil wells to force the leftovers of oil out of the wells and recover more oil (Gaikwad, 2018).

While there are various applications for using CO_2 directly, many are limited to small-scale processes or less demanding products. As a result, the total amount of CO_2 utilized is relatively small compared to the amount of CO_2 released into the atmosphere. A more effective strategy for achieving significant CO_2 reduction on a large scale would be to convert CO_2 into chemicals and alternative fuels or fuel additives (Gaikwad, 2018).

1.1.2.2.2 Conversion of CO_2

As previously stated, CO_2 has various direct uses. However, the potential of CO_2 in direct use is limited compared to its potential when converted to chemicals and fuels via carboxylation or reduction for the synthesis of polycarbonate, synthesis gas, methanol, salicylic acid, and urea. The chemical industry is estimated to make only a small contribution to reducing global CO_2 emissions through direct utilization. It could instead convert approximately 1% of the total global CO_2 emissions into chemical products and up to 10% into synthetic fuels (Erdogan Alper, 2017).

Using CO_2 to produce value-added chemicals and fuel alternatives has multiple benefits, including eco-friendly processing and safer chemical procedures. The high thermodynamic and kinetic stability of CO_2 has limited its usage to its full potential for chemical and fuel synthesis until now. Nevertheless, there have been notable advancements and investments made in CCU start-ups (Gaikwad, 2018). **Table 1.3** displays some of the major routes of CO_2 utilization in various chemical conversion processes, while **Figure 1.3** illustrates venture capital investments in recent years.

Table 1.3: Example of commercial processes producing chemicals form CO_2.

Chemical process	Company
Production of ethylene oxide (C_3-PEO)	RTI International, USA
CO_2 to chemicals and fuels	Liquid Light, USA
Dimethyl carbonate from CO_2 and CH_3OH	E3Tec Service, LLC, USA
Acetic acid synthesis from CO_2 and CH_4	Gas Technology Institute, USA
CO_2 to polyurethane	Bayer with CAT, Germany
CO_2 to renewable methanol (CH_3OH)	Carbon Recycling International, Iceland

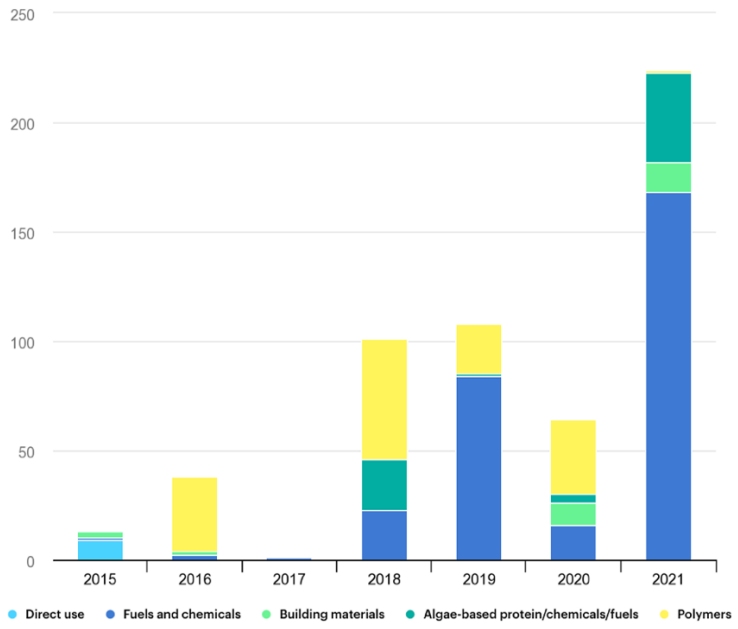

Figure 1.3: Venture Capital investments in CCU start-ups, 2015-2021 (IEA , 2022).

Converting CO_2 into organic compounds involves reactions that utilize the entire molecule. Regarding catalytic CO_2 reduction reactions, CO_2 is transformed into other C1 chemicals, such as CO and methanol. The transformation of CO_2 into fuels, as opposed to organic chemicals, is critical in CO_2 emissions management strategies. This is because the demand for fuels exceeds that for organic chemicals. Moreover, since CO_2 emissions are primarily linked to the use of fossil fuels, fuels produced from CO_2 can replace fossil fuels and aid in the closure of the open carbon cycle. The chemical industry consumes only approximately 10% of the world's crude oil, with the remainder used for liquid fuels like gasoline, diesel, and heavy oil. Therefore, a significant reduction in global CO_2 emissions can only be achieved by effectively utilising CO_2 for fuel production. The conversion of CO_2 to methanol is a promising approach that may provide a complete resolution to the problems of greenhouse gas management and depletion of fossil fuels. Methanol is a precursor for various valuable chemicals and can also serve as a fuel. Furthermore, some studies have proposed that CO_2 can be transformed into C1 to C10 hydrocarbon fuels through methanol, making it highly promising for industrial use (Nam, Kim, Kishan, Choi, & Lee, 1999), (Inui, Kitagawa, Takeguchi, Hagiwara, & Makino, 1993).

Hydrogen production from hydrocarbon reforming is currently the dominant method, accounting for 96% of global hydrogen production. However, this process is energy-intensive and contributes to greenhouse gas emissions and climate change. Nevertheless, there are alternative emerging technologies, such as water splitting using solar light, photoelectrochemical, and photobiological processes, which do not emit carbon dioxide and can be utilized for renewable methanol production (Basile & Dalena, 2018).

1.2 Methanol

This section explores the significance of CO_2 hydrogenation to methanol and provides an overview of the methanol economy. Furthermore, a comprehensive review of the historical background of methanol, its usage, and demand will be presented, along with an analysis of the current advancements in renewable methanol production.

1.2.1 Current Methanol status

Methanol is the world's fifth most significant commodity chemically produced and a primary raw material for the chemical industry. The demand for methanol is expected to grow, considerably in the coming years (**Figure 1.1**) due to increased use of methanol-based fuels and chemicals. This growth is primarily driven by the displacement of oil with methanol, especially in processes like methanol to olefins (MTO) and methanol to propylene (MTP) (Methanol Market, 2021).

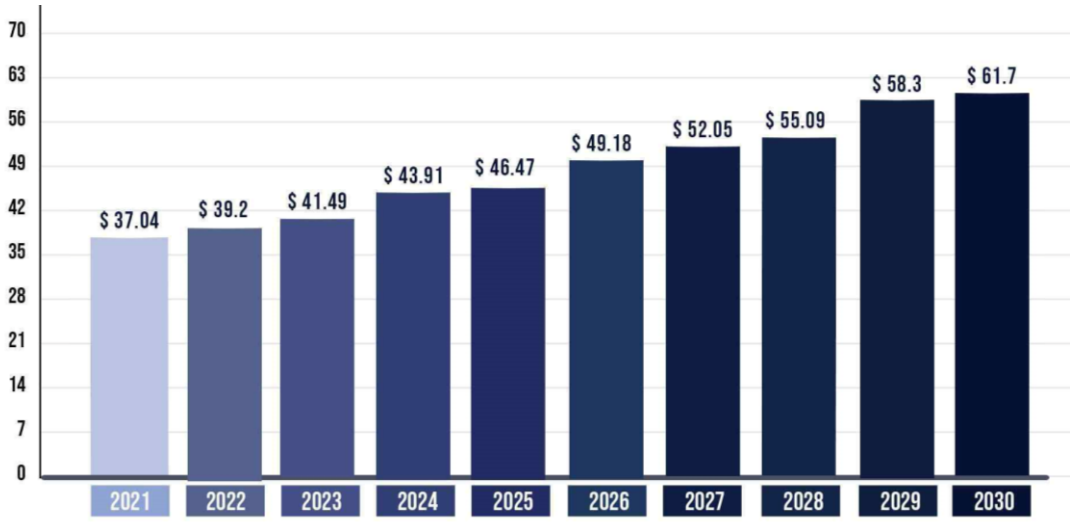

Figure 1.4: Methanol market size, 2021-2030 (USD Billion) (Methanol Market, 2021)

Methanol is a versatile chemical that serves as an essential commodity in producing various materials. Its importance lies in the fact that it can be used as a feedstock for a wide range of chemical products such as formaldehyde, acetic acid, and methyl tert-butyl ether (MTBE), which in turn are used to make a variety of materials, including plastics, adhesives, and solvents (Basile & Dalena, 2018).

Methanol is utilized in the transportation sector as a fuel constituent, either directly in fuel blends or in the form of MTBE in gasoline and FAME (fatty acid methyl ester) in diesel. In several countries, including China, Denmark, Israel, and Australia, mid- and high-level methanol fuel blends have been the subject of recent projects. The consumption of mid- to high-level methanol fuel blends is also expected to grow, predominantly in the Asia-Pacific region (Methanol Institute, 2016).

Methanol has an energy density roughly half that of conventional fuels (Figure 1.5). However, its potential be derived from sustainable sources, making it a suitable intermediary fuel for a transportation industry powered by renewable energy. Methanol-based fuels have several advantages over conventional fuels to meet market and regulatory demands for cleaner energy sources. In addition, due to its cleaner combustion and lower emissions of particulate matter, NO_x, SO_x, and hydrocarbons (Verhelst, Turner, Sileghem, & Vancoillie, 2019), methanol has the potential to meet the strict regulations being proposed to control marine pollution at a reasonable cost, making it a viable option as a marine fuel. (Andersson, 2015).

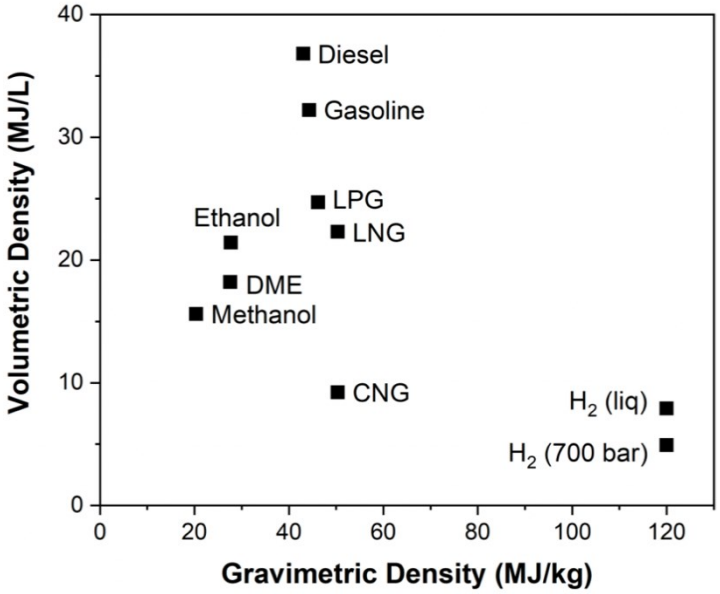

Figure 1.5: Specific energy and energy density of different fuels.

Methanol is a suitable option for the transportation sector due to its widespread global availability, and it is in liquid form at ambient temperatures, making the infrastructure costs relatively low. Additionally, there is an extensive history of handling and using methanol in various applications with established safety protocols. Moreover, methanol is biodegradable, which can reduce the environmental impact in the event of a spill (Basile & Dalena, 2018).

Government regulations on emissions due to environmental concerns are the primary force behind the development of renewable methanol. Additionally, the demand for renewable energy storage could also lead to an increase in the adoption of the CO_2-to-methanol process. Renewable

methanol can be produced from various feedstock sources worldwide, including sustainable biomass or reacting CO_2 with H_2 generated from renewable electricity. However, a sustainable source of hydrogen at a reasonable cost is needed for recycling CO_2 to be economically viable, which can be incentivized by political support.

1.2.2 Methanol synthesis history

In 1661, Irish chemist Robert Boyle isolated pure methanol, but it was not until the 19th century that methanol had any significant use. In 1835, J.B. Dumas and E.M. Peligot identified its chemical and molecular identity and introduced the terms "methyl" and "methyl alcohol." In 1892, its name was changed to methanol in accordance with IUPAC nomenclature. Since then, various attempts have been made to synthesize methanol (Basile & Dalena, 2018).

Towards the end of the 19th century, there was an increasing demand for methanol in the chemical industry, which led to a surge of interest in developing methods for producing it. This led several prominent scientists of the time to work on methanol synthesis technology. In 1905, Paul Sabatier proposed that methanol could be produced by reacting CO and H_2. Copper (Cu) was quickly recognized as a promising catalyst for methanol synthesis. However, the Cu-based catalysts were prone to be poisoned by sulfur impurities in a mixture of CO and H_2 gases, known as syngas (Basile & Dalena, 2018). As a result, at the beginning of 1913, A. Mittasch and M. Pier from BASF successfully produced methanol from CO and H_2 using an iron-based catalyst after the issues with copper-based catalysts being easily poisoned by sulphur impurities. In the 1920s, M. Pier and his colleagues focused on scaling up methanol production and developed a sulfur-resistant catalyst based on ZnO and Cr_2O_3 (Sheldon, 2017). In 1923, the process of producing methanol from CO and H_2 was successfully converted from the development to the production stage at the BASF Leuna Work. The process was based on high pressure (250-350 bar), high temperature (320-450 °C) and the syngas supplied from coal gasification. This method was then used for industrial-scale methanol production for the following four decades (Basile & Dalena, 2018).

Cu-based catalysts were initially unsuitable for methanol synthesis due to the problem of sulphur poisoning. However, with the advent of steam reforming of natural gas, the development of a desulfurization catalyst proved to be a significant breakthrough. This enabled the production of high-purity syngas, which made it possible to utilize Cu-based catalysts for methanol synthesis (Murkin & Brightling, 2016). The use of a highly selective copper/zinc oxide-based catalyst for methanol synthesis was introduced by Imperial Chemical Industries (ICI) in the early 1960s, which was owned and licensed by Johnson Matthey. The catalyst made it possible to operate the process at moderate reaction conditions of 50-100 bar pressure and 200-300 °C temperature. This catalytic process relied on the use of higher purity synthesis gas that was free from sulphur and carbonyl contaminants, which were primarily responsible for catalyst deactivation. As a result, natural gas, which is composed mainly of methane, is the primary feedstock for this process. Presently, this technology accounts for 90% of global methanol production (Basile & Dalena, 2018).

$$CH_4 + H_2O \rightarrow CO + 3H_2 \quad \Delta H_{298K,5MPa} = +206.3 \text{ kJ mol}^{-1}$$

Equation 1.1

As shown in Equation 1.1, Syngas is produced by the decomposition of methane and is subsequently used for methanol synthesis. Research has shown that adding CO_2 in small amounts to the syngas mixture improves the catalytic activity and methanol yield. In modern commercial methanol synthesis processes, up to 30% CO_2 is added to the syngas mixture. However, producing syngas from methane is highly endothermic and requires significant energy. Olah and his colleagues investigated direct methane to methanol synthesis routes. Still, the process proved to have very low yields due to the breakdown of the produced methanol into CO_2 and water at high reaction temperatures of 300 °C (Basile & Dalena, 2018).

Converting CO_2 to methanol through hydrogenation is a promising way to mitigate CO_2 emissions and reduce reliance on fossil fuels by shifting towards renewable energy sources. This can create a closed carbon cycle, which has been proposed as the "Methanol Economy" by G. A. Olah. Renewable methanol can be produced by capturing CO_2 from various sources and directly

converting it into methanol, which is an effective fuel alternative, that is easily stored and transported (Agarwal, 2019) (Olah, 2005).

In recent years, there has been considerable interest in developing effective and sustainable techniques for converting CO_2 to methanol via hydrogenation. The first operational plant for CO_2 hydrogenation was established by Carbon Recycling International (CRI) in Iceland in 2011. Since then, similar facilities have been constructed, with many more currently in the works. Using CO_2 and renewable hydrogen to produce methanol is a promising approach to mitigate greenhouse gas emissions and address climate change while providing a useful chemical feedstock. Consequently, continuous research and advancements in this field have enormous potential for addressing the challenges of sustainable energy and materials production (Agarwal, 2019).

1.2.3 Current status of commercial production of renewable methanol

As mentioned previously, the world's first commercial plant for converting CO_2 into methanol using renewable energy as the source of hydrogen is currently being operated in Iceland by Carbon Recycling International (CRI) (Goeppert, Czaun, Jones, Surya Prakash, & Olah, 2014). The pilot plant, with an initial capacity of 1300 tons of methanol annually relies on the inexpensive and abundant geothermal energy sources available in the area. After an expansion in 2015, the plant produced around 4,000 tons of methanol annually and recycled approximately 5,500 tons CO_2. CRI is now designing and constructing a new plant for emissions-to-liquids to produce methanol from captured CO_2 using surplus electricity from intermittent renewable sources. In October 2022 CRI completed the commissioning of a new CO_2-to-methanol production facility located adjacent to a coke oven gas production (COG) in Anyang city, Henan Province, China. The plant is the world’s largest production of fuel from captured CO_2 emissions with a capacity of 110,000 tons of low-carbon intensity methanol per year (Carbon recycling international, 2022).

Large-scale production of renewable methanol is also achieved through the utilization of solid waste and biomass. Enerkem company, for instance, has devised a process that involves extracting and reutilizing carbon from non-recyclable waste to produce renewable methanol. In 2017, Enerkem successfully produced approximately 60,000 tons of renewable methanol. Another

company based in the Netherlands, BioMCN, operates a facility in Delfzijl with a capacity of 900,000 tons, where they produce renewable methanol from biogas (Studt, et al., 2015).

Södra has implemented a wood-based bio-methanol production process, which commenced operation in 2021 at the Södra Cell Mönsterås pulp mill located in southeastern Sweden (Tada, et al., 2018). Currently, there are numerous low carbons, bio-based method in development to produce methanol from CO_2. The success of these plant highlights the importance of having an affordable source of CO_2 and access to cheap renewable energy for hydrogen production. The methanol produced at the George Olah renewable methanol plant, known as Vulcanol, is currently blended with gasoline. While this is a positive development, there are still issues with the conventional $Cu/Zn/Al_2O_3$-based catalyst used for direct CO_2 hydrogenation to methanol, such as selectivity and stability, that must be addressed to improve efficiency. Developing a more effective catalyst is crucial to the growth of a methanol economy, where methanol is used as fuel or a source of hydrogen and a sustainable cycle of CO_2 utilization.

1.2.4 Reaction chemistry and equilibrium thermodynamics

Carbon dioxide (CO_2) is a molecule with high thermodynamic stability, indicated by its standard Gibbs free energy change (ΔG°) of -394.38 kJ/mol. This negative value signifies that the formation of CO_2 from its elements (carbon and oxygen) is a highly favourable process, indicating the molecule's inherent stability. To activate and convert CO_2 into more valuable compounds, such as methanol, substantial energy input, efficient catalysts, and controlled reaction conditions are necessary (Gaikwad, 2018). The synthesis of methanol from CO_2 or CO takes place according to the reactions below:

CO_2 Hydrogenation (Reaction 1):

- Reaction: $CO_2 + 3H_2 \rightleftharpoons CH_3OH + H_2O$

Equation 1.2

- ΔH° (Standard Enthalpy Change) =-49.5 kJ/mol
- This reaction is exothermic (ΔH° is negative) since it releases 49.5 kJ of heat per mole of CO_2 converted to methanol.

- The drawback of this reaction is the formation of water (H_2O) as a by-product, which can lead to catalyst deactivation due to water's inhibitory effect on the catalyst's active sites.

CO Hydrogenation (Reaction 2):

- Reaction: $CO + 2H_2 \rightleftharpoons CH_3OH$

Equation 1.3

- $\Delta H° = -90.5$ kJ/mol
- Like Reaction 1, this reaction is exothermic and releases 90.5 kJ of heat per mole of CO converted to methanol.
- Notably, there is no formation of water in this reaction, which makes it a preferred route for methanol synthesis, as it avoids the catalyst deactivation issue caused by water.

Reverse Water Gas Shift (RWGS) (Reaction 3):

- Reaction: $CO_2 + H_2 \rightleftharpoons CO + H_2O$

Equation 1.4

- $\Delta H° = 41.2$ kJ/mol
- Reaction 3 is endothermic ($\Delta H°$ is positive), indicating that it requires an input of 41.2 kJ of heat per mole of CO_2 converted to CO and H_2O.

As for the thermodynamic behaviour of the reactions in **Equation 1.2** and **Equation 1.3** are both exothermic processes that release heat during methanol formation. In these exothermic reactions, the heat generated can potentially be used to drive the reaction forward. However, Reaction 1 has the drawback of water formation, which can reduce the catalyst's activity.

To maximize the conversion of CO_2 into methanol through Reaction 1, high-pressure and low-temperature conditions are recommended. Le Châtelier's principle suggests that these conditions favour higher methanol production in exothermic reactions like the hydrogenation of CO_2 to methanol. The management of temperature and pressure, along with the choice of suitable catalysts, plays a vital role in the industrial production of methanol from CO_2 or CO while considering the thermodynamic aspects of these reactions (Stangeland, 2021).

1.2.5 Catalysts development of CO_2 hydrogenation to methanol

Currently, most commercial methanol synthesis processes rely on a ternary catalyst composed of $Cu/ZnO/Al_2O_3$. This catalyst is typically synthesized using the coprecipitation method. Johnson Matthey, Sudchemie, Haldor Topsoe, and BASF are leading catalyst producer companies. The molar concentration of each component in the $Cu/ZnO/Al_2O_3$ catalyst typically falls within the range of CuO = 50-70%, ZnO = 20-50%, and Al_2O_3 = 5-20%. (Álvarez, et al., 2017).

Several factors influence the catalytic properties during the synthesis process. Factors such as the mixing of precursors, precipitation, and subsequent treatments including aging, washing, drying, calcination, and reduction, can significantly impact the resulting microstructure of $Cu/ZnO/Al_2O_3$ catalysts (Gaikwad, 2018). Figure 1.6 illustrates the pellets and particles of commercially available methanol synthesis catalysts from Alfa Aesar (Product ID: 45776).

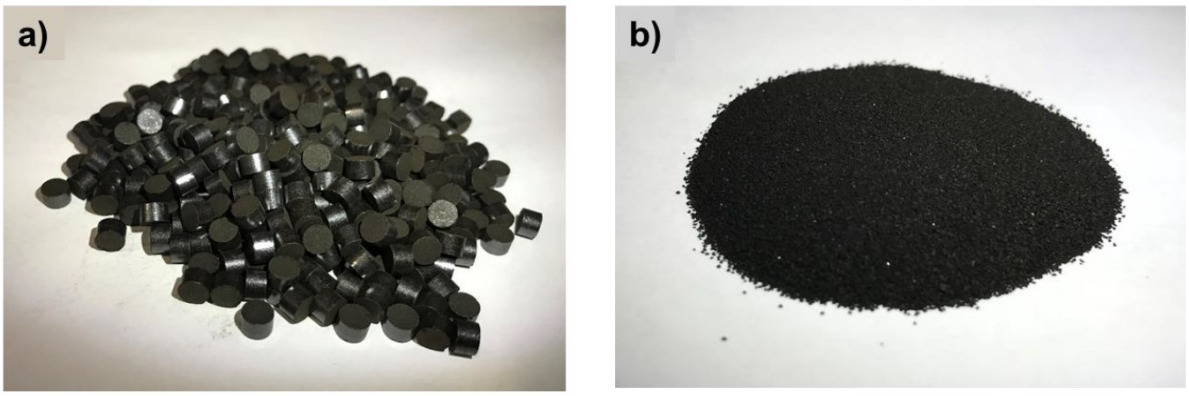

Figure 1.6: Commercial $Cu/ZnO/Al_2O_3$ catalyst from Alfa Aesar a) Catalyst pallets b) crushed and sieved 100-300 µm particle size.

It has been agreed upon that alumina plays a role as a structural promoter in the catalytic system. As a result, it stabilizes the system and prevents sintering, allowing for high copper particle dispersions which is essential for achieving high performance, as it has been found to have a linear relationship with activity (Li & Chen, 2019) (Stangeland, 2021).

The primary challenge associated with the conventional $Cu/ZnO/Al_2O_3$ catalyst is its moderate methanol selectivity and rapid water-induced sintering. There is little evidence of the active play role of Al_2O_3 in the reaction. To further improve the catalysts in terms of activity, selectivity, or stability, researchers have explored the incorporation or substitution of various metal oxides such as Zn, Zr, Ce_2O_3, La_2O_3, Ga_2O_3, Y_2O_3, TiO_2, and SiO_2 (Nakamura, et al., 1996) (Kattel, Ramírez, Chen,

Rodriguez, & Liu, 2017) (Kuld, et al., 2016) (Senanayake, et al., 2016) (Liao, et al., 2011) (Amenomiya, 1987).

The catalysts Cu/Zn and Cu/ZrO_2 have been shown to exhibit good yield and selectivity for methanol production, respectively. Consequently, the addition of both ZnO and ZrO_2 to Cu has been extensively studied as a means of producing catalysts with enhanced activity and selectivity (Li & Chen, 2019). $Cu/Zn/ZrO_2$ (CZZ) catalysts have been reported to outperform $Cu/Zn/Al_2O_3$ catalysts, although the synergistic effects between the components are still subject to debate. ZrO_2 possesses higher oxygen storage capacity, surface area, active sites, and thermal stability than Al_2O_3, which contribute to the maintenance of the redox cycle of the catalyst during the reaction and contribute to improved catalyst performance. Furthermore, ZrO_2's hydrophobic properties make it a more suitable support material than Al_2O_3. Al_2O_3's high affinity for water can result in the deactivation of active sites and catalyst sintering, which could negatively impact catalytic performance (Stangeland, 2021).

Extensive academic and industrial research has been conducted to further improve the performance of CZZ catalysts by incorporating a fourth and fifth element (Li & Chen, 2019). Recently, there has been growing interest in utilizing graphene and related materials like graphene oxide (GO) and reduced graphene oxide (rGO) as catalyst supports and carbon catalysts. This is mainly due to their advantageous characteristics, including a large surface area, exceptional thermal and chemical stability, ease of surface modification, and the presence of diverse, active sites (Li & Chen, 2019).

Extensive research has been conducted on Pd-based catalysts; however, their widespread industrial implementation is limited by the relatively higher cost of Pd. The interface between Pd and oxide species and alloying with metals such as Zn or Ga are crucial factors in developing high-performance catalysts for methanol synthesis using Pd (Martin, et al., 2016). Moreover, there has been growing research interest in In_2O_3-based catalysts based, primarily due to their remarkable methanol selectivity, even at elevated temperatures ranging from 200 to 320 °C. Oxygen vacancies in In_2O_3 play a vital role in facilitating the activation and conversion of CO_2 into methanol. Studies have shown that the catalytic activity of In_2O_3 can be enhanced by incorporating additional metal oxides (such as ZrO_2 and Y_2O_3) and metals like Pd, Ni, and Cu. These additives promote the

formation of oxygen vacancies and improve H_2 activation, thereby contributing to improved catalyst performance (Chou & Lobo, 2019). Although the addition of ZrO_2 to Ln_2O_2-based catalysts as a support has been reported to yield 100% selectivity, the activity and efficacy of methanol synthesis remain limited and inadequate for industrial use (Martin, et al., 2016).

1.3 Scope of this work

1.3.1 Scientific objectives

The primary objective of this research project is to advance the field of CO_2 hydrogenation to methanol by the development and assessment of novel catalysts enhanced through the incorporation of EAGs. This investigation encompasses not only the synthesis and characterization of these catalysts but also a rigorous exploration of the profound effects that the introduction of EAGs may impact upon their catalytic performance. The overarching aim is to contribute to a deeper understanding of the synergistic interactions between EAGs and traditional catalysts in the context of CO_2 conversion to methanol, with the aspiration of enhancing this critical chemical transformation's catalytic efficiency and providing a strategy for mitigating CO_2 emissions.

1.3.2 Outline

This thesis is organized into five chapters, followed by the reference and appendix sections. This chapter (Chapter 1) introduces the current scenario of CO_2 emissions, its impact on lifestyle, and mitigation strategies. Furthermore, an overview of methanol history, renewable methanol and current CO_2 hydrogenation to methanol catalysts are provided.

Chapter 2 deeply explains common industrial catalysts, their active site, and their reaction mechanism. It also investigates the influence of adding a new element, especially graphene oxide.

Chapter 3 introduces background information on catalyst preparation, the materials characterization techniques, analytical methods, and the reactor used to collect and analyze the data presented in this dissertation. Specifically, physical, and chemical characterization techniques, spectroscopic techniques, and an experimental setup for catalyst evaluation are described in the chapter.

Chapter 4 presents the result of characterization experiments on newly developed catalysts.

Chapter 5 summarizes the key conclusions of the thesis, highlights its relevance, and is complemented by an outlook for future research directions.

References and Appendices are presented at the end of this thesis.

CHAPTER 2 Literature review

Catalysts for CO_2 hydrogenation can be categorized into four groups depending on the active metal involved: traditional copper (Cu) catalysts, palladium (Pd) catalysts, indium oxide (In_2O_3) catalysts, and other catalysts composed of transition metals. The performance of catalysts that convert CO_2 into methanol relies heavily on the presence of metal oxides and the formation of alloys. However, the exact mechanism behind the interaction between the various components of the catalyst is not yet fully comprehended. This lack of understanding can be attributed to the complex and dynamic nature of these systems, which presents a significant challenge in determining the specific role played by different phases. Copper-based catalysts have garnered significant attention due to their ease of manufacturing, cost-effectiveness, and notable performance. Furthermore, prior studies have demonstrated that copper outperforms other active metal components for CO_2 hydrogenation to methanol (Fan, 2021).

$$Cu >> Co = Pd = Re > Ni > Fe >> Ru = Pt > Ir = Ag = Rh > Au$$

This section provides an overview of the pertinent studies related to the experimental segment of this research, which primarily focuses on copper-based catalysts. Specifically, the discussion will encompass research on cupper-based catalysts and the impact of various promoters, such as ZnO, ZrO_2, graphite oxide, and EAGs, on the catalysts' efficacy. Additionally, an examination of the reaction mechanism will be presented.

2.1 CO_2 hydrogenation to methanol over Cu-based catalysts

The catalytic activity is significantly improved by having a large surface area of copper. The specific copper surface area and particle size are important factors affecting the catalytic performance. Smaller particles lead to better dispersion and reduced agglomeration, resulting in improved catalytic activity. Consequently, the catalyst was supported on a metal oxide to achieve both high activity and stability simultaneously (Baltes, Vukojević, & Schüth, 2008) (Lee, Moon, Lee, Lee, &

Kim, 1995) (Solomon, Jones, & May, 1993). Moreover, the catalytic performance is influenced by the synergistic effects that result from the interaction between copper and metal oxides. Extensive research has been carried out on copper-based catalysts, which incorporate different modifiers or promoters such as zinc (Zn), zirconium (Zr), cerium (Ce), gallium (Ga), aluminum (Al), silicon (Si), vanadium (V), and titanium (Ti) (Wang, Wang, Ma, & Gong, 2011). Among these, the Cu-ZnO and Cu-ZrO2 catalyst has been extensively studied for CO_2 hydrogenation reactions due to their high activity and selectivity (Li & Chen, 2019).

2.2 Active sites of Cu/ZnO

Cu or ZnO alone had little effect on methanol synthesis (Karelovic, Bargibant, Fernández, & Ruiz, 2012). However, the combination of Cu and ZnO enhanced the catalyst performance dramatically (Gesmanee & Koo-Amornpattana, 2017). The active phase in Cu/ZnO catalysts has been a subject of debate for many years and continues to be a topic of intense research. The suggested promotional effects of ZnO on Cu include (1) enhancing the presence of highly active Cu metal surfaces, (2) decorating the Cu surface with Zn or ZnO_x species, (3) formation of Cu-ZnO interfacial sites, and (4) reverse spillover of hydrogen from ZnO, where ZnO acts as a hydrogen reservoir (Abbas, Kim, Shin, Yoon, & Jung, 2019).

Concerning proposal (1), Cu lattice strain and defects have been recognized as a sign of heightened activity, and the presence of the ZnO phase can influence this aspect (Kasatkin, Kurr, Kniep, Trunschke, & Schlögl, 2007) (Behrens, et al., 2012). Additionally, studies have revealed that the activity of Cu(100) is similar to that of unoptimized Cu/ZnO catalysts (Rasmussen, et al., 1994) (Chorkendorff, Rasmussen, & Kazuta, 1994). Strong evidence suggests that the activity of copper surfaces can be significantly enhanced by decorating them with Zn or ZnO_x, in relation to proposal (2). Researchers led by Nakamura showed a significant increase in the turnover frequency (TOF) by several orders of magnitude when Zn was applied to Cu(111) and polycrystalline Cu surfaces (Fujitani, Nakamura, Ueno, Uchijima, & Nakamura, 1997) (Nakamura, et al., 1996). (Kuld, et al., 2016) noted that methanol turnover frequency (TOF) rises as the amount of Zn on Cu surfaces

increases in an industrial-style $Cu/ZnO/Al_2O_3$ catalyst. Additionally, (Senanayake, et al., 2016) demonstrated that the activity of Cu surfaces decorated with ZnO was approximately twice as high as that of Cu nanoparticles deposited on the ZnO surface. (Kattel, Ramírez, Chen, Rodriguez, & Liu, 2017) discovered that the Zn components were easily oxidized to ZnO_x during the reaction, which enhanced the activity. More recently, during the process of CO_2 hydrogenation to methanol, a blend of Zn or ZnO_x formate was identified through in situ analysis under conditions relevant to industrial applications (Zabilskiy, et al., 2020). The enhanced impact of these Zn or ZnO_x species is believed to be due to their ability to stabilize the formate intermediate and promote the hydrogenation process of formate into methanol (Behrens, et al., 2012) (Zabilskiy, et al., 2020) (Fujitani, Nakamura, Ueno, Uchijima, & Nakamura, 1997). Therefore, the presence of Zn or ZnO_x formate species on Cu is crucial in creating a high number of active sites in Cu/ZnO-based catalysts. Additionally, the proximity of Cu and Zn facilitates the formation of these species on the surface of Cu (Zabilskiy, et al., 2020). Proposal (3) suggests that the existence of oxygen vacancies at the interface between Cu and ZnO plays a role in facilitating the activation and hydrogenation of CO_2 into methanol (French, Sokol, Bromley, Catlow, & Sherwood, 2003) (Liao, et al., 2011). Therefore, it is crucial to optimize both the Cu-ZnO interface and the interfacial area to maximize the activity of Cu/ZnO-based catalysts in methanol synthesis.

ZnO has been shown to play an important role in providing active sites for the spillover of hydrogen during the hydrogenation of carbon dioxide to methanol. According to several studies, including (Waugh, 1992) (Gesmanee & Koo-Amornpattana, 2017), and (Hu et al. ,2018), ZnO can act as a hydrogen storage material and facilitate the transfer of hydrogen species to the active sites on the catalyst surface. The active sites for the spillover of hydrogen species on ZnO can include surface defects, steps, edges, and vacancies, as well as Cu-ZnO interfaces. These sites can enhance the adsorption, diffusion, and dissociation of hydrogen species, as well as their transfer to the Cu-based catalysts.

2.3 Active sites of Cu/ZrO_2

It is believed that Cu species interacting with oxide supports serve as active sites for CO_2 and H_2 conversion, and the support material significantly impacts the selectivity of methanol. ZrO_2 as a support plays a crucial role in the mechanism and can be considered an integral part of the "active site". It is worth highlighting that at one bar pressure, Cu/ZrO_2 with low Cu loading (1–2 wt. %) possesses comparable methanol yields as the $Cu/ZnO/Al_2O_3$ (45–50 wt % Cu) catalysts (Denise, Cherifi, Bettahar, & Sneeden, 1989). (Amenomiya, 1987) compared binary catalysts, including Cu/ZnO, Cu/ZrO_2, Cu/TiO_2, Cu/SiO_2, and Cu/Al_2O_3 for CO_2 hydrogenation to methanol and found that the CuO/ZrO_2 catalyst showed the highest unit mass activity and selectivity. (Nitta, Suwata, Ikeda, Okamoto, & Imanaka, 1994) observed that Cu-ZrO_2 is more effective in producing methanol from CO_2 than Cu-ZnO, especially at high temperatures (>200 °C). They concluded that ZrO_2 plays a more crucial role in selective methanol production than ZnO. On the other hand, (Kanoun, Astier, & Pajonk, 1992) proposed that ZrO_2 in Cu/ZrO_2 catalysts promotes the dispersion of Cu and interacts with metallic Cu to create active sites for the selective synthesis of methanol.

The presence of interfacial sites primarily determines the activity of Cu/ZrO_2 catalysts. These catalysts typically function as bifunctional catalysts, where Cu facilitates the dissociative adsorption of H_2, while CO_2 activation and the subsequent hydrogenation of intermediates occur at the interfacial sites. (Polierer, Jelic, Pitter, & Studt, 2019) recently found that the intermediates are too strongly adsorbed on the Cu/ZrO_2 interface and ZrO_2 phase for further conversion to methanol. Instead, the beneficial impact of ZrO_2 was attributed to the electronic promotion of Cu surface sites located in proximity to the ZrO_2 phase.

The influence of different phases of ZrO_2 on the catalytic activity of Cu/ZrO_2 catalysts is discussed in several related references (Li, Mao, Yu, & Guo, 2015) (Liu, Wang, Wang, & Yang, 2005) (Jung & Bell, 2002) (Tada, et al., 2018) (Samson, et al., 2014). The results of these references consistently demonstrate that amorphous ZrO_2 is advantageous for stabilizing small Cu particles, and its interaction with small Cu particles leads to high methanol selectivity and CO_2 conversion. However, the crystallization of amorphous ZrO_2 can cause the partial deactivation of catalysts, and the increase in Cu particle size can decrease CO_2 conversion while promoting methanol selectivity. While some publications suggest that the crystal forms of ZrO_2 (monoclinic and tetragonal) are also closely related to catalytic performance, there is no agreement on this matter. For example, both

t-ZrO_2 and m-ZrO_2 have been found to enhance methanol synthesis by altering the formation of oxygen vacancies or modifying surface properties.

2.4 Influence of metal oxide promoter/additive on Cu-based catalysts

Cu–ZnO and Cu–ZrO_2 are the most promising catalysts for CO_2 hydrogeneration to methanol. Although the catalytic performance of Cu/ZnO and Cu/ZrO_2, which are obtained through different methods, varies, it is widely accepted that Cu/ZrO_2 is more effective in selectively producing methanol from CO_2. At the same time, Cu/ZnO has higher activity in converting CO_2 (Li & Chen, 2019). In this situation, combining the two is logical to create a new ternary catalyst. The resulting Cu/ZnO/ZrO_2 catalyst demonstrates highly efficient performance in forming methanol due to the multiple interactions between the Cu species and ZnO-ZrO_2 oxides.

Ternary oxides often show synergistic effects from the interactions of different components. Regardless of the preparation methods, reaction temperatures, and Gas Hourly Space Velocity (GHSVs), the Cu/ZnO/ZrO_2 ternary catalysts exhibit significantly higher catalytic activity than Cu–ZnO and Cu–ZrO_2, especially at lower temperatures (180-240°C) (Arena, et al., 2007) (Arena, et al., 2008) (Yang, et al., 2006) (Witoon, et al., 2018).

Additionally, the Cu/ZnO/ZrO_2 catalyst also shows enhanced methanol productivity compared to the Cu/ZnO/Al_2O_3 and Cu/ZnO/CeO_2 catalysts due to the substantial modification of textural and chemical properties, such as specific surface area, Cu dispersion, and Cu surface area, and improved adsorption properties brought about by ZrO_2 (Arena F. , et al., 2013) (Arena F. , et al., 2013) (Bonura, et al., 2011). Comparison between Cu/ZnO/ZrO_2 and Cu/ZnO/Al_2O_3 reveals the importance of the weak hydrophilic character of the ZrO_2 support to benefit the desorption of produced water and thermodynamically promotes the formation of methanol (Arena, et al., 2007). The atomic-level interaction between Cu, ZnO, and ZrO_2 is relatively complex and has yet to be extensively studied in situ. The interface between ZnO and ZrO_2 can convert the carbonate intermediate into more reactive species, such as formate (Li & Chen, 2019) (Wang, et al., 2019) (Abbas, Kim, Shin, Yoon, & Jung, 2019). The enhanced performance of Cu/ZnO/ZrO_2 catalysts,

compared to bimetallic catalysts (Cu/ZnO and Cu/ZrO_2), has been attributed to the reverse spillover of hydrogen from ZnO. This reverse spillover process amplifies the methanol synthesis rate at the interfacial sites of Cu/ZrO_2.

Extensive investigations have been conducted on incorporating additional elements into $Cu/ZnO/ZrO_2$ catalysts, and it has been found that carbon-based materials positively influence catalytic efficiency (Li & Chen, 2019). For instance, adding carbon nanofibers as support increases the rate of methanol synthesis by increasing the amount of dispersed copper on the surface (Din, Shaharun, Subbarao, & Naeem, 2015) (Din, Shaharun, Naeem, Tasleem, & Johan, 2017). Nitrogen-containing modified Cu/ZrO_2 catalysts are more effective in converting CO_2 due to increased dissociation of H_2 and CO_2 adsorption capability from nitrogen-containing functional groups (Wang, et al., 2015) (Sun, et al., 2018). Adding the right amount of graphene oxide to a $Cu/ZnO/ZrO_2$ catalyst also leads to a higher yield of methanol and improved selectivity than a catalyst without graphene oxide (Witoon, et al., 2018). The enhancement of hydrogen spillover from the copper surface to oxides through graphene oxide nanosheets acts as a bridge, improving the performance of all catalysts supported by GO (Witoon, et al., 2018) (Zhang, et al., 2010).

2.5 Reaction mechanism over Cu-based catalysts

Despite the extensive research conducted on the reaction mechanism of methanol synthesis using Cu-based catalysts, there are still unanswered questions regarding the chemical nature of the active sites and the mechanism of methanol formation. The proposed reaction mechanisms for the hydrogenation of CO_2 to methanol can be categorized into two main groups: the formate mechanism and the RWGS (Reverse Water Gas Shift) reaction, which involves the production of CO followed by CO hydrogenation to methanol (known as the RWGS + CO hydrogenation pathway).

The essential inquiries that need to be answered can be addressed through the following questions: (1) Which intermediates, and elementary steps are crucial in the process of CO_2 hydrogenation to methanol (2) what is the rate-determining step (3) What roles do metal and metal oxides play in the mechanism (4) Can CO generated from the RWGS reaction undergo further hydrogenation to produce methanol (5) Which sites are responsible for the formation of CO.

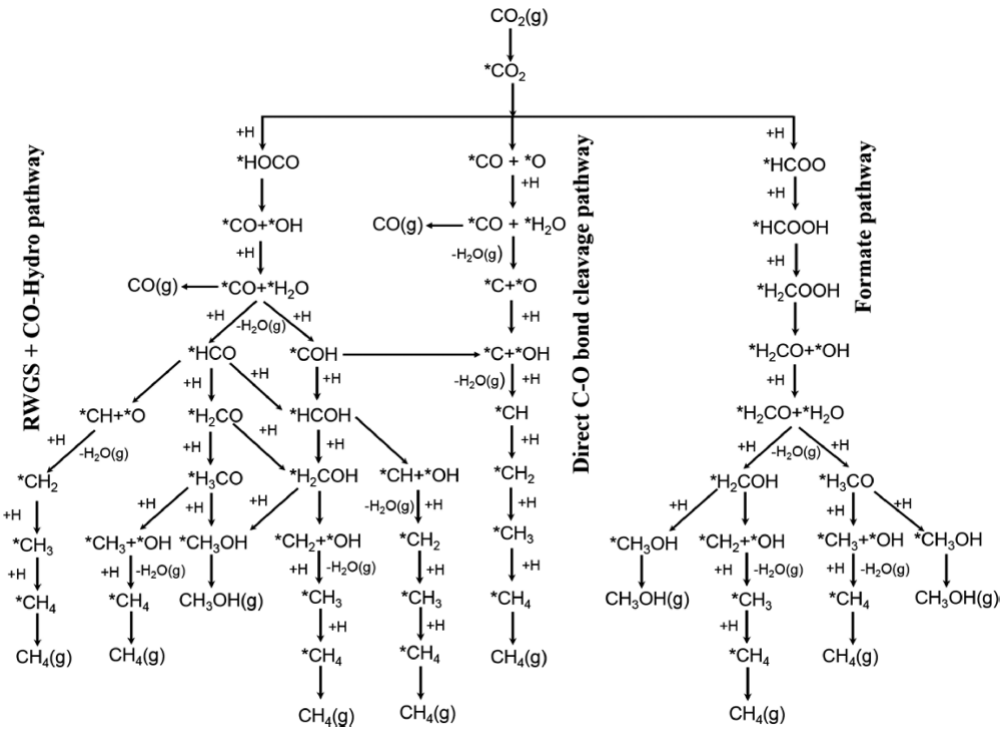

*Figure 2.1: Possible reaction pathways of CO_2 hydrogenation to CO, CH_3OH, and CH_4. *(X) indicates adsorbed species (Kattel, Ramírez, Chen, Rodriguez, & Liu, 2017).*

Mechanistic studies on the synthesis of methanol from CO_2 using Cu/ZnO and Cu/ZrO_2 catalysts predominantly support the direct formation of methanol from CO_2 through the involvement of formate intermediates. This conclusion is backed by experimental evidence from isotopic labelling experiments and in situ transient kinetic experiments (Kunkes, Studt, Abild-Pedersen, Schlögl, & Behrens, 2015) (Larmier, et al., 2017) (Kattel, Ramírez, Chen, Rodriguez, & Liu, 2017).

The extensive research conducted by (Larmier, et al., 2017) provides compelling evidence that methanol synthesis from CO_2 over Cu/ZrO_2 catalysts takes place through the involvement of the formate intermediate under relevant reaction conditions. However, studies conducted at lower pressures have indicated that methanol production occurs through the RWGS + CO hydrogenation pathway over Cu/ZrO_2 catalysts (Kattel, Yan, Yang, Chen, & Liu, 2016) (Schild, Wokaun, & Baiker, 1991) (Weigel, Koeppel, Baiker, & Wokaun, 1996).

The RWGS + CO hydrogenation pathway has also been suggested for CeO_x/Cu(111) and Cu/TiO_2 catalysts (Graciani, et al., 2014) (Kattel, Yan, Yang, Chen, & Liu, 2016). The reaction pathway can be

influenced by the specific conditions of the reaction, stressing the importance of investigating catalytic systems under realistic operational conditions (Yang, Mims, Mei, Peden, & Campbell, 2013).

According to (Bartholomew & Farrauto, 2011) the process of methanol synthesis from syngas is believed to predominantly proceed through a series of steps involving CO_2* → HCOO* → H_2COO* → H_3CO* → H_3COH*. Among these steps, the hydrogenation of H_2COO was identified as the rate-determining step (H_2COO* + H* ⇌ H_3CO* + O*).

Most experimental and computational investigations into the reaction mechanism on Cu/ZnO and Cu/ZrO_2 catalysts also provide evidence that methanol is generated through a comparable reaction pathway. However, it is commonly observed that CO_2 reacts with an HCOO formation via an Eley-Rideal (ER) mechanism. Density functional theory (DFT) calculations have identified H_2CO as an intermediate in the formate route. Therefore, regarding question 1, studies indicate that the reaction pathway on Cu/ZnO and Cu/ZrO_2 catalysts involves the following sequence:

CO_2(g) + H* → HCOO* → H_2COO* → H_2COOH* → H_2CO* → H_3CO* → H_3COH*.

Regarding the second question, most studies also indicate that the rate-determining step is either the hydrogenation of HCOO or H_2COO (Stangeland, 2021). The proposed roles of different metal oxides in addressing question 3 contain several aspects:

(i) Enhancing CO_2 activation (Reichenbach, et al., 2018) (Zheng, Narkhede, Han, Zhang, & Li, 2020) (Tao, et al., 2019).

(ii) Stabilizing reaction intermediates (Behrens, et al., 2012) (Fujitani, Nakamura, Ueno, Uchijima, & Nakamura, 1997) (Morikawa, Iwata, & Terakura, 2001)

(iii) Reducing the energy barrier of reaction steps (Kattel, Ramírez, Chen, Rodriguez, & Liu, 2017) (Reichenbach, et al., 2018) (Martínez-Suárez, Siemer, Frenzel, & Marx, 2015) (Martínez-Suárez, Frenzel, Marx, & Meyer, 2013) (Martínez-Suárez, Frenzel, & Marx, 2014).

(iv) Facilitating electron transfer from the Cu surface to metal oxide (Polierer, Jelic, Pitter, & Studt, 2019) (Catlow, French, Sokol, & Thomas, 2005) (Yang, et al., 2017).

(v) Creating new, more favourable reaction pathways through Cu-oxide interfacial sites, which provide sites for a portion or the entire reaction mechanism (Zheng, Narkhede, Han, Zhang, & Li, 2020) (Wang, et al., 2019) (Larmier, et al., 2017) (Tao, et al., 2019).

Multiple studies have indicated that a combination of pathways is involved in the conversion of CO_2 to methanol, with several phenomena (i-v) likely contributing to the synergistic effect between Cu and oxide species. These phenomena are potentially chemically interconnected.

In the methanol synthesis process from CO_2 using Cu/Zn/ZrO_2, there are several key steps: (1) The adsorption and dissociation of H_2 on metal sites, (2) the transfer of hydrogen atoms from one surface to another, (3) the rapid diffusion of hydrogen atoms across the oxide surface, and (4) the reaction or exchange of hydrogen atoms with other intermediates. Due to the complexity of the ternary components, an agreement has not been reached regarding the active sites and pathways for the mentioned key steps.

A formate pathway with a dual-site or bifunctional mechanism has been proposed for CO_2 hydrogenation to methanol over CZZ catalysts. As shown in Figure **2.2** (a), hydrogen adsorption and dissociation occur on the Cu site. Then atomic hydrogen is transferred from the surface of Cu to the active sites of oxides, such as the hydroxyl groups of ZrO_2 and basic Lewis sites of ZnO, to react with adsorbed CO_2 and form formate and other intermediates, ultimately leading to the production of methanol. This pathway involves ZnO and ZrO_2 interacting separately with Cu to perform hydrogenation reactions (Arena, et al., 2008) (Bonura, Cordaro, Cannilla, Arena, & Frusteri, 2014). Another investigation highlights the role of ZnO–ZrO_2 interaction in the adsorption and conversion of CO_2, as shown in Figure **2.2** (b). In situ DRIFTS measurements under atmospheric or high pressure (3 MPa) suggest that the ZnO–ZrO_2 interface is the active site for CO_2 adsorption to carbonate species and its conversion to formate, while the Cu sites contribute to the subsequent hydrogenation process. DFT calculations suggest that the formation of the ZnO–ZrO_2 interface can promote *HCOO activation, which has been suggested to control the reaction rates at the Cu/ZnO and Cu/ZrO_2 interfaces during CO_2 hydrogenation (Wang, et al., 2019).

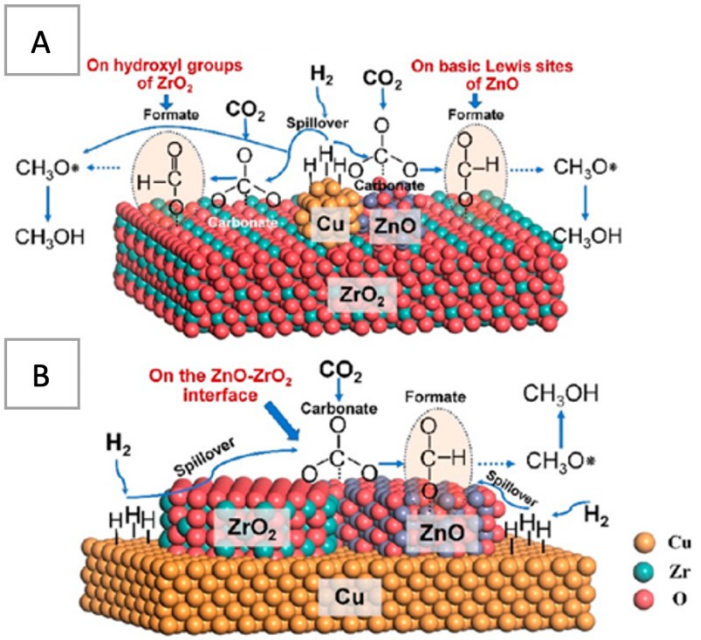

Figure 2.2: Possible reaction pathways and active sites of CO_2 hydrogenation to CH_3OH over, the Cu/ZnO/ZrO_2 (a) (Arena, et al., 2008) (b) (Wang, et al., 2019).

2.6 Enhancing catalytic performance: investigating the effects of graphite in Cu-based catalysts

There are various studies on the hydrogenation of CO_2 to methanol using different graphene-based catalysts. These catalysts encompassed few-layer graphene (FLG), reduced graphene oxide (rGO), nitrogen-doped graphene in others, and oxide-graphene composites with oxide components such as Al_2O_3, ZrO_2, or ZrO_2-Al_2O_3. Considering that all these catalysts consisted of multiple components, the preparation methods exhibited significant variations (as outlined in

Table 2.1). Each method aimed to achieve optimal interaction between CuO, ZnO, ZrO_2, the additional oxide, and graphene to obtain the desired materials.

Table 2.1: Graphene-based catalysts for CO_2 hydrogenation to methanol

Catalysts	Properties of the Catalysts	Reaction Condition	Ref
CuO-ZnO-Al_2O_3-rGO_x x: 5; 10 and 15 wt.%	For CuO-ZnO-Al_2O_3-rGO (10 wt.%) S_t = 147 m^2/g S_{Cu} = 12.6 m^2/g_{cu} Cu dispersion = 9.4%	Reduction in H_2; 280 °C; 6 h H_2/CO_2 = 3:1 T = 250 °C P = 30 bar GHSV = 12,000 $mL.g^{-1}.h^{-1}$	(Liu, Tang, Xu, & Wang, 2014)
CuO-ZnO-Al_2O_3-N-rGO_x x = 7; 10; 13 and 16 wt.%	For CuO-ZnO-Al_2O_3-N-rGO (10 wt.%) S_t = 102 m^2/g S_{Cu} = 58.3 m^2/g Cu dispersion = 8.6%	Reduction in (H_2 + N_2); 300 °C; 6 h H_2/CO_2 = 3:1 T = 200 °C P = 30 bar W/F = 10 g. h. mol^{-1}	(Ma, Geng, Zhang, Zhang, & Zhao, 2018)
CuO-ZnO-ZrO_2-rGOx x = 0.5; 1; 2.5; 5 and 10 wt.% of GO	For CuO-ZnO-ZrO_2-GO(1 wt.%) S_t = 145 m^2/g S_{Cu} = 25.3 m^2/g Cu dispersion = 11.2% actual GO wt.% = 1.4	Reduction in H_2; 300 °C; 4 h H_2/CO_2 = 3:1 T = 200–280 °C P = 20 bar	(Witoon, et al., 2018)
CuO-ZnO-ZrO_2-Al_2O_3-rGO mixed oxides: 20 wt.%	St = 125 m^2/g S_{Cu} = 1.9 m^2/g	Reduction in (H_2 + N_2); 300 °C; 2 h H_2/CO_2 = 3:1 T = 200–280 °C P = 10–20 bar GHSV = 6075–10,935 h^{-1}	(Fan & Wu, 2016)
CuO-ZnO-N-rGO 10 wt.% CuO-ZnO Cu:Zn = 1:1	S_t = 80 m^2/g	Reduction in H_2; 300 °C; 30–180 min H_2/CO_2 = 3:1 T = 250 °C P = 15 bar GHSV = 2400 h^{-1}	(Deerattrakul, Limphirat, & Kongkachuichay, 2017)
CuO-ZnO-N-rGO(3D) 15 wt.% CuO-ZnO Cu:Zn = 1:1 N-rGO with 3D structure	For N-rGO catalyst reduced with urea St = 110 m^2/g Oxide NPs size = 7–8 nm	Reduction in H_2; 300 °C; 1.5 h H_2/CO_2 = 3:1 T = 250 °C P = 15 bar GHSV = 2444 h^{-1}	(Deerattrakul, Yigit, Rupprechter, & Kongkachuichay, 2019)
CuO-ZnO-N-rGO 5; 10; 20 and 30 wt.% CuO-ZnO Cu:Zn = 1:1	For the catalyst with 10 wt.% oxides content St = 83 m^2/g	Reduction in H_2; 350 °C; 1.5 h H_2/CO_2 = 3:1 T = 200–300 °C P = 15 bar GHSV = 2400 h^{-1}	(Deerattrakul, Dittanet, Sawangphruk, & Kongkachuichay, 2016)
CuO-ZnO-rGO(3D) 5; 10; 15 and 20 wt.% CuO-ZnO Cu:Zn = 1:1 r-GO with 3D structure	For the catalyst with 15 wt.% CuO-ZnO and rGO reduced at 140 °C St = 140 m^2/g Oxide NPs size = 7–8 nm	Reduction in H_2; 350 °C; 1.5 h H_2/CO_2 = 3:1 T = 250 °C P = 15 bar GHSV = 2444 h^{-1}	(Deerattrakul, Puengampholsrisook, Limphirat, & Kongkachuichay, 2018)

	oxidation states of Cu and Zn for all catalysts are close to Cu^0 and Zn^{2+}		
Cu-ZnO-rGO Cu:Zn = 1:1	Cu crystallite size = 37 nm	H_2/CO_2 = 3:1 T = 200–240 °C P = 30 bar WHSV = 6.6 h^{-1}	(San, et al., 2021)
Cu-ZnO-rGO from HKUST-1 Cu:Zn = 1.2:1	Cu crystallite size = 27 nm Cu NP size = 25 nm	H_2/CO_2 = 3:1 T = 200–240 °C P = 30 bar WHSV = 6.6 h^{-1}	(San, et al., 2021)
Cu-Ni-rGO metal-support mass ratio = 1:10 Cu:Ni = 2:1	bimetallic Cu-Ni NPs of 20 nm Cu—mix of Cu^0, Cu^+ and Cu^{2+} Ni—only Ni^{2+} the presence of Ni promotes the Cu reduction	Reduction in (H_2 + N_2); 270 °C; 2 h H_2/CO_2 = 3:1 T = 225 °C P = 40 bar GHSV = 2500 h^{-1}	(Wang, et al., 2021)
Cu-Ni-N-rGO metal-support mass ratio = 1:10 Cu:Ni = 2:1	bimetallic Cu-Ni NPs of 50 nm Cu—mix of Cu^0, Cu^+ and Cu^{2+} Ni—only Ni^{2+} the presence of Ni inhibits the reduction of Cu	Reduction in (H_2 + N_2); 270 °C; 2 h H_2/CO_2 = 3:1 T = 225 °C P = 40 bar GHSV = 2500 h^{-1}	(Wang, et al., 2021)

The first study to investigate the use of graphene-based materials for CO_2 hydrogenation to methanol was published in 2014 and utilized CuO-ZnO-Al_2O_3-rGO. To prepare the catalyst, rGO was mechanically mixed with CuO-ZnO-Al_2O_3 mixed oxides that were synthesized using coprecipitation method. The two components were closely connected by ball-milling the solid mixture (Liu, Tang, Xu, & Wang, 2014). Another CuO-ZnO-ZrO_2-Al_2O_3-rGO catalyst was prepared by mixing GO with CuO-ZnO-ZrO_2-Al_2O_3 mixed oxides in a liquid phase using N-methyl-pyrrolidone (Fan & Wu, 2016). Sample catalysts of CuO-ZnO-Al_2O_3-N-rGO and CuO-ZnO-ZrO_2-rGO were prepared by co-precipitating mixed oxides in the presence of graphene, followed by a calcination process. In the case of CuO-ZnO-Al_2O_3-N-rGO, the co-precipitation of oxide precursors occurred in the presence of N-rGO (Ma, Geng, Zhang, Zhang, & Zhao, 2018). For CuO-ZnO-ZrO_2-rGO, the oxides and graphene oxide were simultaneously thermally reduced after co-precipitation (Witoon, et al., 2018).

To prepare CuO-ZnO-rGO(3D) and CuO-ZnO-N-rGO with 2D or 3D structures, $Cu(NO_3)_2$ and $Zn(NO_3)_2$ were impregnated onto graphene derivatives (GO, rGO, or N-rGO), followed by

calcination in air (Deerattrakul, Puengampholsrisook, Limphirat, & Kongkachuichay, 2018) (Deerattrakul, Dittanet, Sawangphruk, & Kongkachuichay, 2016) (Deerattrakul, Limphirat, & Kongkachuichay, 2017).

A recent publication by (San, et al., 2021) describes a new technique to produce highly uniform Cu dispersed on graphene. This method, called "Template Genetic Inheritance" or “TGI” involves synthesizing the Cu-containing metal-organic framework (MOF) named HKUST-1 on the surface of graphene, followed by its gradual thermal decomposition to produce CuO and then $Cu.Zn(NO_3)_2$ was also included in the preparation process to obtain ZnO, resulting in a final catalyst of Cu-ZnO-rGO. Graphene played a crucial role in providing a large surface area for HKUST-1 dispersion and acted as a carbon source for in-situ CO reduction of CuO formed after MOF decomposition. In the study by the (Wang, et al., 2021), $Cu(NO_3)_2$ and $Ni(NO_3)_2$ were impregnated onto rGO and N-rGO, followed by a reduction in 5% H_2/N_2 at 300 °C to prepare a bimetallic Cu-Ni catalyst without ZnO. The reduction temperature is too low to entirely reduce Cu or Ni, resulting in a mixture of oxidic and metallic Cu and Ni on the reduced graphene oxide support. Although the resulting catalyst is unusual, CO_2 conversion at medium temperatures (225 °C) and high pressures (40 bar) were low, but the methanol selectivity was among the highest reported so far.

The CO_2 conversion and methanol selectivity values reported for graphene-supported catalysts are shown in Figure 2.3. However, it is difficult to directly compare the results due to significant differences in the catalysts composition and testing conditions. Figure 2.3 and

Table 2.1 provide a general overview of the activity of graphene-supported catalysts. The first observation is that some of these materials show improved CO_2 conversion and especially significantly better selectivity for methanol formation than the classic oxide-supported catalysts usually employed for CO_2 hydrogenation for which 5–20% conversions and CH_3OH selectivity of up to 80% were reported (Din, Shaharun, Alotaibi, Alharthi, & Naeem, 2019).

The second significant finding is that nitrogen-doped graphene supports exhibit better catalytic performance in converting CO_2 to methanol than the undoped carbon materials. This result can be explained by the fact that, in addition to enhancing CO_2 adsorption and H_2 dissociation, N species, especially in the form of pyridinic-N, promote the reduction of CuO (Deerattrakul, Yigit,

Rupprechter, & Kongkachuichay, 2019)). Furthermore, pyridinic-N attracts hydrogen donor molecules, positively affecting the reaction pathway for CO_2 conversion to methanol (Deerattrakul, Dittanet, Sawangphruk, & Kongkachuichay, 2016). The third observation is that the catalyst prepared using the TGI method (Cu-ZnO-rGO) showed significantly better CO_2 conversion and CH_3OH selectivity values than the impregnation catalyst. According to the authors, this improvement can be attributed to the synergistic effect of graphene and HKUST-1, which enhances the surface area, Cu reducibility, and adsorption capacity of H_2 and CO_2. However, the paper did not provide quantitative measurements to support these claims (San, et al., 2021).

The mentioned studies conclude the role of graphene support in the CO_2 hydrogenation to CH_3OH both the support and promoter in the catalysts. As a support, it aids in the dispersion of Cu. At the same time, as a promoter, graphene acts as a bridge between the Cu surface and the surfaces of the oxides (ZnO and ZrO_2), which are not in direct contact with the metal, facilitating the transfer of activated species. Its presence enhances the spillover of H* from the Cu surface to meet activated CO_2 species (mostly formate) situated at the Cu-oxide interface and those adsorbed on the isolated oxide nanoparticles. This promotes the utilization of more catalytically active sites in the hydrogenation process compared to the graphene-free catalyst, in which isolated sites for CO_2 adsorption cannot interact with activated hydrogen and thus cannot participate in the reaction. Moreover, nitrogen-doped graphene provides the basic sites that improve CO_2 adsorption and CO_2 transfer to the active sites.

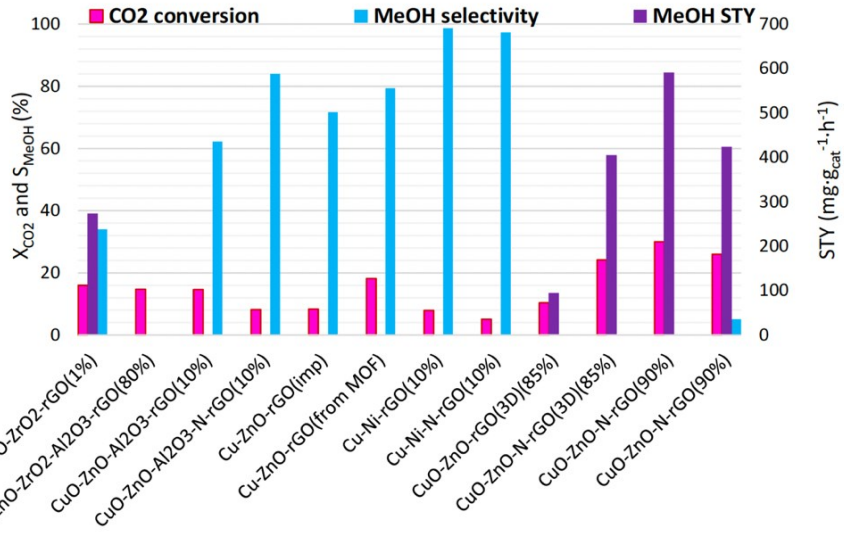

Figure 2.3: The results of CO_2 hydrogenation to methanol catalyzed by graphene derivative supported catalysts (Mihet, Dan, & Lazar, 2020).

CHAPTER 3 Experimental Methods

The objective of this chapter is to provide a comprehensive overview of the following aspects: 1) the method adopted for the activating EAGs and synthesis of metal oxide catalysts, 2) The characterization methods utilized to determine the physicochemical properties of the catalysts, including textural, structural, reducibility, and morphological characteristics, 3) The design considerations for a flow reactor, safety measures, and the evaluation procedure for determining reaction quantities.

3.1 Sample Preparation

3.1.1 Materials and Chemicals

Table 3.1 summarizes the chemicals and materials used in this thesis.

Table 3.1 Summary of materials and chemicals used in this thesis.

Chemical	Chemical formula	Supplier
EAG	-	-
Nitric acid (66%)	HNO_3	Sigma-Aldrich
Copper (II) nitrate trihydrate	CuN_2O_6. $3H_20$	Sigma-Aldrich
Zinc nitrate hexahydrate	N_2O_6Zn. $6H_2O$	Sigma-Aldrich
Zirconium (IV) oxynitrate hydrate	N_2O_7Zr. xH_2O	Sigma-Aldrich
Sodium carbonate	Na_2CO_3	Sigma-Aldrich

* All the materials and chemicals were used as received without further purification

3.1.2 Catalyst synthesis

The co-precipitation approach has gained significant popularity as a methodology for nanoparticle synthesis due to its simplicity, efficiency, and versatility. This technique involves precipitation reactions occurring between dissolved ionic compounds in a solution. The resulting product(s) comprises at least one insoluble component that undergoes nucleation and subsequent growth processes. The synthesis of desired nanoparticles requires careful regulation of the reaction conditions such as temperature, pH values, aging time, and reactant concentrations. Following the completion of the reaction, the resulting mixture is filtered and subjected to calcination, producing as-prepared metal oxides that can function as effective catalysts (Petrucci, 2007). The filtration stage is performed to eliminate undesirable impurities, while the subsequent calcination process involves applying heat to the mixture, resulting in a thermodynamically stable product. These as-prepared metal oxides exhibit favourable surface properties, including a high surface area, homogeneity, and reactivity, making them suitable catalysts for various applications (Rase, 2000).

The X%-Cu/ZN/Zr/EAGs catalysts were synthesized through a co–precipitation method. X represents the total mass percentage of EAGs, and the ratio Cu/Zn/Zn is 6/3/1. The performance of a catalyst is significantly affected by the metal oxide ratio employed. Consequently, the ratio above has been chosen on account of its demonstrated efficacy in prior studies. To synthesize the catalysts, predetermined quantities of metal salts of $Cu(NO_3)_2.3H_2O$, $Zn(NO_3)_2.6H_2O$, and

$ZrO(NO_3)_2 \cdot xH_2O$ were initially dissolved in 250 mL of deionized water (Solution A), followed by the dissolution of the desired amount of 0.2 M sodium carbonate in 250 mL of deionized water (Solution B). In parallel, F-EAGs were dispersed in 50 mL of de-ionized water and heated to 70 °C under intense stirring (Solution C). Subsequently, Solutions A and B were slowly added dropwise into Solution C, and the mixture was stirred for 3 hours at 400 rpm, resulting in the formation of metal carbonate precipitates, as described by Equation 3.1-3.3. The resulting mixture was aged at room temperature for an hour, filtered, and washed with 2000 mL of deionized water until the pH of the filtrate reached 6.5±0.2. The residues were then dried in the air at 120 °C for 16 hours with a heating ramp of 2 °C.min^{-1}, ensuring uniform calcination. The calcination of the samples was performed in the air at 350 °C for 4 hours with a heating ramp of 2 °C.min^{-1}, Which result in pre-reduced catalysts consists of CuO, ZnO and ZrO_2, as depicted by Equation 3.4-3.6.

$$Cu(NO_3)_2 + 2NaCO_{3(S)} \rightarrow CuCO_{3\,(s)} + 2NaNO_{3\,(aq)} + CO_{2\,(g)} + H_2O$$

Equation 3.1

$$Zn(NO_3)_{2\,(S)} + 2NaCO_{3(S)} \rightarrow ZnCO_{3\,(s)} + 2NaNO_{3\,(aq)} + CO_{2\,(g)} + H_2O$$

Equation 3.2

$$ZrO(NO_3)_{2\,(S)} + 2NaCO_{3(S)} \rightarrow ZrOCO_{3\,(s)} + 2NaNO_{3\,(aq)} + CO_{2\,(g)} + H_2O$$

Equation 3.3

$$CuCO_{3\,(s)} \xrightarrow{calcination} CuO_{(s)} + CO_{2(g)}$$

Equation 3.4

$$ZnCO_{3\,(s)} \xrightarrow{calcination} ZnO_{(s)} + CO_{2(g)}$$

Equation 3.5

$$ZrOCO_{3\,(s)} \xrightarrow{calcination} ZrO_{2(s)} + CO_{2(g)}$$

Equation 3.6

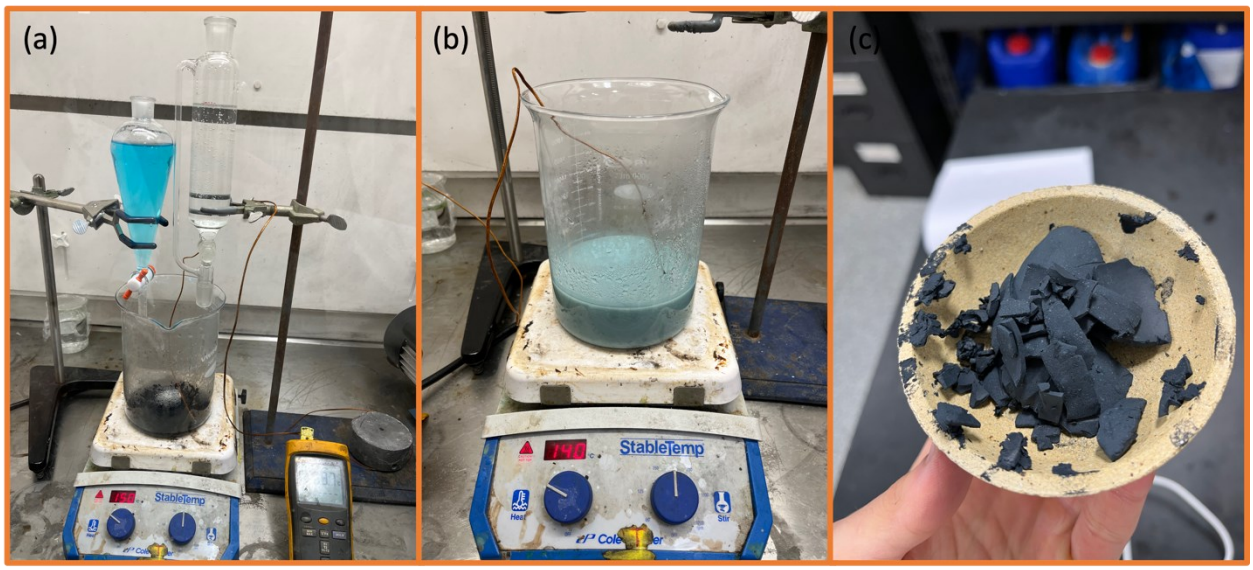

Figure 3.1: A graphical illustration of the different steps involved during the synthesis of Cu/Zn/Zr/EAGs catalysts (a) deposition–precipitation setup, (b) prepared solution, (c) Filtered catalyst.

3.2 Characterization Experiment

3.2.1 X-Ray Diffraction (XRD)

The textural properties of calcined catalysts were assessed using the powder X-ray diffraction (XRD) technique. The measurements were conducted at room temperature in ambient air, employing a Bruker D8 Advance High-Speed X-ray Diffractometer. Cu Kα irradiation (with a wavelength of 1.5405 nm, Kα1 only) was utilized within the 2θ range of 10.0° to 90.0°. The XRD measurements were carried out with a voltage of 30 kV, a current of 10 mA, and a step size of 0.02° (with a time of 2 seconds per step). These measurements took place in the Mechanical Engineering Department at Dalhousie University.

Powder X-ray Diffraction (XRD) is employed to analyze the atomic structure of crystalline materials. This technique serves two main purposes: (i) Identifying nano-crystalline phases by comparing peak positions with standard ICDD files for X-ray diffraction, (ii) Estimating the coherent size of crystal domains (Skoog, Holler, & Crouch, 2018).

In 1912, Bragg established that constructive interference of X-rays from a series of parallel planes only occurs at specific angles θ. This angle θ is determined by the X-ray wavelength and the interplanar spacing of the material, as depicted in Figure **3.1**. This relationship is described by Bragg's law (Equation 3.7). It should be noted that the portion of X-ray photons that are not scattered continues through to the subsequent layer of atoms, where another portion of the X-rays is scattered (Chou, 2019).

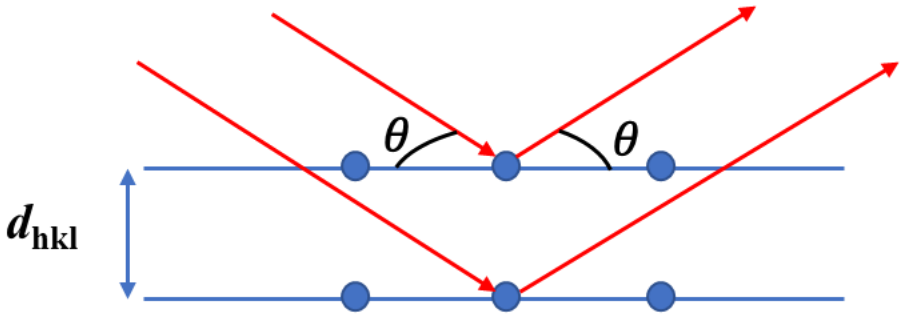

Figure 3.1: Illustration of the beams diffracted by two different layers (Chou, 2019).

$$2d_{hkl}\sin\theta = n\lambda$$

Equation 3.7

Where:

d_{hkl}: distance between two planes of the same crystallographic family (Å) with indices hkl.

θ: peak position, angle between incident X-ray beam and solid surface which is the first layer of diffraction objects (multiplied by π and divided by 180, expressed in radians)

n: integer number of path lengths, equal to 1 with the used diffractometer

λ: X-ray wavelength equal to 1.5418 Å (since we are using the Kα ray of Cu)

XRD typically utilizes X-ray wavelengths ranging from 0.1 Å to 25 Å, which allows for consistency in measurements. An XRD chart is a visual depiction of the diffraction pattern resulting from the interaction of an X-ray beam with a crystalline material. The chart displays the intensity of diffracted X-rays (y-axis) as a function of the diffraction angle (2θ) (x-axis). By comparing the peak positions

with standard ICDD files, it becomes possible to identify nano-crystalline phases (Skoog, Holler, & Crouch, 2018).

The Scherrer formula (Equation 3.8) was applied to determine the coherent size of crystal domains, which is assumed to be equal to the mean diameter of particles. This assumption holds true primarily for extremely small crystalline sizes, as observed in the investigated catalysts. This estimation is based on measuring the full width at half maximum of a specific diffraction peak (Skoog, Holler, & Crouch, 2018).

$$D_{hkl} = K.\lambda / \beta . \cos\theta_{hkl}$$

Equation 3.8

Where:

D_{hkl}: average nanocrystals size (Å)

K: Shape factor set at 0.9 for spherical particles

λ: X-ray wavelength equal to 1.5405 Å

β: full width at half maximum (FWHM) of the diffraction peak (dimensionless)

θ_{hkl}: peak position, angle between incident beam and solid surface (multiplied by π and divided by 180, expressed in radians)

XRD played a significant role in this thesis by examining the catalyst's structure. For instance, the XRD technique was employed to identify the crystalline phases of metal oxides.

3.2.2 N_2 physisorption

Nitrogen adsorption-desorption isotherms were measured using a Quantachrome Nova 4200e analyzer, which determines surface area and pore size. These experiments took place at Dalhousie University's Chemistry Department. Before each measurement, catalyst samples (300-400 mg) were subjected to vacuum degassing at 150°C for 3 hours to eliminate any residual solvents or molecules that could either be physically adsorbed (e.g., H_2O) or chemically adsorbed (e.g., CO_2) (Jabbour, 2020).

The technique operates based on assessing the gas adsorption (specifically nitrogen in this instance) over a degassed powder sample, volumetrically and at a constant temperature (-196°C, the temperature of liquid nitrogen). This measurement is conducted by examining the adsorption of the gas in relation to its relative pressure (P/P_0). The adsorption occurs due to secondary forces, typically weak van der Waals forces, involving mono-surface nitrogen adsorption or multi-layered nitrogen-nitrogen interactions. By recording measurements at various relative pressures, following both increasing and decreasing P/P_0 patterns, it becomes possible to construct an adsorption-desorption isotherm, as illustrated in Figure **3.2** (Lowell, Shields, Thomas, & Thommes, 2004).

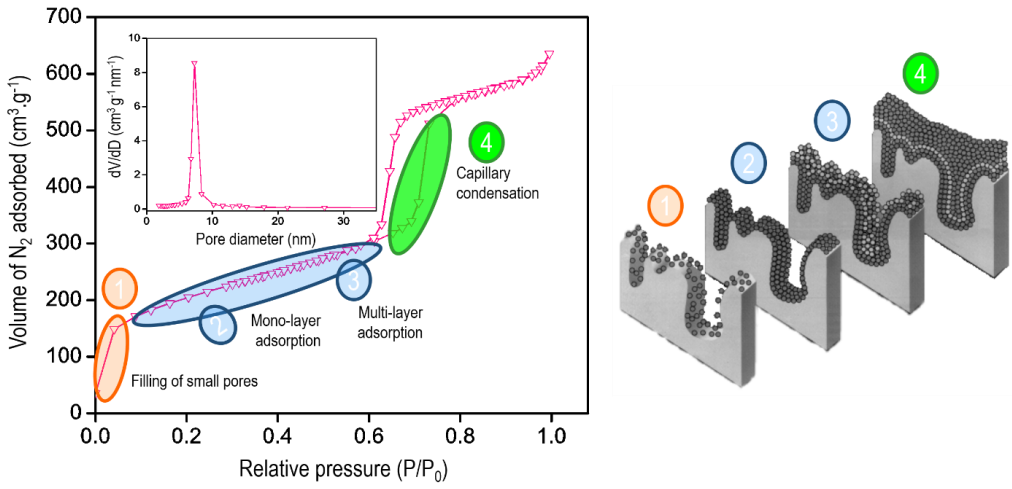

Figure 3.2: N_2 sorption isotherm (on the right) and pore size distribution (inset figure) of calcined SBA-15 support accompanied by a schematic representation (on the left) illustrating the different stages involved during N_2 adsorption over porous material (Jabbour, 2020).

The adsorption process unfolds in several stages. Initially, smaller micropores are filled (1), followed by the formation of a monolayer (2) and subsequent development of multilayers of nitrogen (N_2) (3) on all accessible surfaces. As the multilayer thickens, there is a rapid increase in the volume of absorbed N_2, which corresponds to capillary condensation occurring within mesopores (4). Eventually, a linear section is observed, indicating the formation of a thick multilayer on the external surface. Interestingly, when the adsorption behaviour differs from the desorption behaviour, a hysteresis loop is formed, as shown in Figure **3.2**, within the relative pressure range

of 0.6-0.8 P/P_0 (Lowell, Shields, Thomas, & Thommes, 2004) (Brunauer, Deming, Deming, & Teller, 1940).

Through a comprehensive examination of literature conducted by (Brunauer, Deming, Deming, & Teller, 1940), the IUPAC developed a classification in 1985 that enables the differentiation of various types of porous materials and the characterization of six sorption isotherms. According to this classification, microporous solids are defined as materials possessing the smallest pores, with an average diameter below 2 nm. Mesoporous materials confine pores ranging from 2 to 50 nm in size. Lastly, macroporous materials are characterized by the widest pores, which have openings greater than 50 nm. Moreover, the shape of the isotherm depends greatly on the type of the material (Sing, 1985).

The examination of the N_2-sorption isotherm offers valuable textural data, the specific surface area (analyzing the mono-layer range), pore size distribution, and pore volume (representing the total volume of N_2 adsorbed at a relative pressure of 0.99 P/P_0). Additionally, it provides insights into pore uniformity and offers quantitative information regarding microporosity, mesoporosity, and macroporosity (Lowell, Shields, Thomas, & Thommes, 2004). The specific surface area refers to the overall surface available for N_2 molecules to interact with, it is worth noting that extremely small micropores may not always be accessible to N_2 (Kruk & Jaroniec, 2001). It is measured in units of square meters per gram (m^2/g) and encompasses both internal and external (between grain) porosities.

In the present study, the surface area was evaluated within a relative pressure range (P/P_0) of 0.05 to 0.25, focusing on the adsorption of N_2 at the monolayer level. The surface area value was calculated using Equation 3.9, originally proposed by Brunauer, Emmet, and Teller (BET) (Brunauer, Emmett, & Teller, 1938).

$$\frac{C}{V.(P_0 - P)} = \frac{1}{V_M} + \frac{(C-1)P}{V_M.P_0}$$

Equation 3.9

Where:

P: nitrogen equilibrium vapor pressure, expressed in Pa (Pascal)

P_0: saturation vapor pressure (Pa) at the experimental temperature (-196°C)

V: volume of gas adsorbate (ml) at standard temperature and pressure (STP, 0°C and 1.013 x 105 Pa) at a given value of P

V_M: volume adsorbed (ml) at monolayer coverage

C: thermodynamic parameter (dimensionless) associated to the interaction of N_2 molecule and the surface. This parameter is related to N_2 heat of adsorption as a function of the solid surface, as represented by the relationship in Equation 3.10.

$$C = \exp\left[\frac{\Delta HA - \Delta HL}{R.T}\right]$$

Equation 3.10

Where:

ΔH_A: heat of adsorption of N_2 ($J.mol^{-1}$)

ΔH_L: heat of liquefied nitrogen (719.3 $J.mol^{-1}$)

R: universal gas constant (8.314 J. K-1. mol^{-1})

T: absolute temperature (273 K)

In practical terms, a plot of $C/V(P-P_0)$ against P/P_0 was generated, which results in a linear relationship. This line intersects the primary y-axis at $1/V_M$ and has a slope of $(C-1/V_M)$, allowing for the determination of the thermodynamic parameter C. By utilizing the obtained V_M value, we can calculate the BET specific surface area (S_{BET}) using Equation 3.11.

$$S_{BET} = \frac{V_M.N_A.A_M}{V.M}$$

Equation 3.11

Where:

V_M: the volume adsorbed at monolayer coverage (mL)

N_A: Avogodro's number (6.023x1023 molecules/mol)

A_M: cross sectional area of the adsorbate molecule (0.162 x 10-18 m^2/molecule of N_2) and m is the mass (g) of the tested powder.

It is important to acknowledge that various assumptions are made when utilizing the BET equation to calculate surface area. These assumptions include considering a homogeneous surface for the material and assuming that nitrogen molecules are adsorbed linearly, horizontally, across the surface (Lowell, Shields, Thomas, & Thommes, 2004).

The pore size distribution (PSD) of all materials was determined by analyzing the adsorption branch of the N_2-sorption isotherm. The improved Kelvin method, which relies on the Barrett-Joyner-Halenda (BJH) method, was employed for this purpose (Barrett, Joyner, & Halenda, 1951).
The BJH method (Equation 3.12) assumes that: (1) Pores of the same radius exhibit similar behavior in response to changes in relative pressure, (2) Pores reach liquid N_2 condensation at a relative pressure of 0.99 (during the condensation stage), (3) After complete filling, each pore's surface contains a physiosorbed layer of adsorbate molecules with a statistically determined thickness and an inner capillary volume. During the desorption stage, evaporation commences as the relative pressure decreases (Barrett, Joyner, & Halenda, 1951).

$$V_{pn} = R_n + \Delta V_n - R_n . \Delta t_n . f_i . \sum_{j=1}^{n-1} A_{pj}$$

Equation 3.12

Where:

V_{pn}: pore volume of the nth pore (ml)

R_n: radius and is equal to $r_{pn}^2/(r_{kn} + \Delta t_n)^2$ where r_{pn} is the pore width of the nth pore and r_{kn} is the internal pore volume of the pore after occurrence of multilayer adsorption (m)

ΔV_n: change in pore volume from the nth to n-1 step (ml)

Δt_n: change in statistical thickness of the nth pore during the nth desorption step (m)

f_i: an approximate correction factor for pores of different sizes values and is based on the pore radius (dimensionless)

A_{pj}: average area from which adsorbed gas is desorbed from step j to n-1 (m^2)

After obtaining the pore size distribution through nitrogen physisorption data analysis, it becomes possible to determine the average pore size. However, it is worth noting that this method may result in underestimating the actual pore size by approximately 20%. To achieve more precise values, alternative models utilizing modulation techniques have been proposed and utilized in previous literature, such as NLDF (Nonlocal Density Functional) and Monte Carlo simulation theories. These advanced approaches offer more accurate estimations of pore sizes. (Jabbour, 2020).

The single-point BET method operates under the assumption that the entire adsorption isotherm can be represented by a single data point, usually obtained at low relative pressures. This data point is utilized to calculate the surface area using the BET equation. Although the single-point BET method is convenient and efficient, it may not accurately reflect the actual surface area for materials possessing complex pore structures and multiple types of surface sites. In contrast to the single-point BET method, the multiple-point BET method considers the entire adsorption isotherm by fitting the BET equation to multiple data points. This approach provides greater accuracy but necessitates more data and may require a more extended analysis time. The decision between using the single-point or multiple-point BET method depends on the complexity of the material under examination and the desired level of accuracy (Lowell, Shields, Thomas, & Thommes, 2004). For relatively straightforward materials like this thesis catalysts, the single-point BET method may be satisfactory and has been employed consistently throughout the experiments (Großmann, 2013).

The pore volume at a single point was determined by assessing the amount of nitrogen adsorbed at a relative pressure of 0.98, assuming the complete filling of all pores with a liquid adsorbate. The total volume of adsorbed nitrogen was subsequently converted to the volume of liquid nitrogen contained within the pores, utilizing Equation 3.13 (Kruk & Jaroniec, 2001).

$$V_{iq} = \frac{P.V_{ads}.V_{Mo}}{m.R.T}$$

Equation 3.13

Where:

V_{iq}: volume of liquid nitrogen (ml)

P: nitrogen equilibrium vapor pressure (Pa)

V_{ads}: volume of adsorbed nitrogen (ml)

V_{Mo}: molar volume of liquid adsorbate (34.7 ml.mol^{-1} for N_2)

R: universal gas constant (8.314 J. K^{-1}. mol^{-1})

T: absolute temperature (273 K) and m is the mass (g) of the tested powder

3.2.3 Scanning Electron Microscopy (SEM) and Energy Dispersive X-ray (EDX) Spectroscopy

The scanning electron microscope (SEM) enables the examination and characterization of solid materials morphology at the nanoscale. This technique typically provides images on a scale ranging from nanometers (nm) to micrometers (µm). Topographical images in SEM are created using back-scattered primary or low-energy secondary electrons. SEM proves particularly valuable in the study of non-crystalline catalysts, as it allows for the detailed analysis of mesopore distribution and sizes (Chou, 2019).

SEM observations were performed in the Mechanical Engineering Department of Dalhousie University. The SEM micrographs were captured using a Hitachi S-4700 SEM microscope, operating at an electron acceleration voltage of 20 kV. Like a transmission microscope, an EDS spectroscope was employed alongside the SEM for local chemical analyses. For sample preparation, a small quantity of powder was placed onto an alumina support and coated with a thin silver. This silver layer facilitated the flow of electrostatic charges through the slightly conductive materials when exposed to irradiation. Multiple spots of the sample were examined and acquired at various magnifications to ensure representative images.

The fundamental principle of this technique relies on detecting secondary electrons emitted from the sample's surface when it is bombarded by a scanning primary electron beam. The resulting SEM images typically have a resolution of less than 5 nm. Other interactions between the primary electrons and the sample are also considered, including the emission of backscattered electrons, the adsorption of primary electrons by the solid surface, and the generation of excited X-ray photons, which can sometimes be close to visible light photons. These various interactions yield supplementary information about the topography and surface composition of the studied material

(Jabbour, 2020). In this specific situation, examining SEM images provides valuable data regarding three aspects: (i) the general morphology of the sample, (ii) the distribution and arrangement of metal oxide nanoparticles, and (iii) the visualization of EAGs on the catalysts.

SEM can be combined with energy-dispersive X-ray spectroscopy (EDX), a technique known as SEM-EDX. In this approach, the sample is bombarded with an electron beam, resulting in the emission of X-rays from the material. These emitted X-rays are then measured using an energy-dispersive spectrometer. EDX allows for quantitatively determining the elemental composition since the X-ray energies are specific to particular atoms. However, it is essential to note that the accuracy of EDX measurements may be low. During the analysis, it is crucial to carefully examine if the characteristic peaks of the elements in the dispersive spectra overlap to avoid erroneous reporting (Skoog, Holler, & Crouch, 2018).

EDX is commonly referred to as semi-quantitative analysis in determining the chemical composition and should be utilized as supplementary data for elemental information. In this case, EDX was employed to validate the presence of the metal precursor in the catalyst and to compare it with the nominal metallic concentration of the catalyst.

3.2.4 Inductively Coupled Plasma Mass Spectrometry (ICP-MS)

Inductively Coupled Plasma Mass Spectrometry (ICP-MS) is an effective analytical method for characterizing catalysts, offering precise and sensitive elemental composition data. Prior to conducting ICP-MS analysis on catalysts, it is essential to prepare the samples meticulously to ensure the accuracy and representativeness of the obtained results regarding the catalysts. The sample preparation typically involves digesting the catalyst in an acid mixture to dissolve the sample matrix and release the metal species. The choice of acid mixtures may vary depending on the catalyst's characteristics and the specific elements of interest. Subsequently, the resulting solution is diluted with a solvent to adjust the analyte concentrations within the range detectable by the instrument (Skoog, Holler, & Crouch, 2018). ICP-MS instruments generally comprise three primary elements: a sample introduction system, an ICP source, and a mass spectrometer. The sample introduction system introduces the sample solution into the plasma, where it undergoes

ionization and transforms into a mixture of ions in the gas phase. The ICP source employs argon gas to generate a high-temperature plasma responsible for ionizing the sample (Skoog, Holler, & Crouch, 2018).

The mass spectrometer is employed to separate and detect ions based on their mass-to-charge ratio (m/z). The resulting mass spectra offer insights into the elemental composition of the catalyst. The data acquired through ICP-MS analysis can be utilized to determine the catalyst's elemental composition, encompassing the concentrations of metals, carbon, and other elements present. Various software packages can be utilized to process the data and derive quantitative outcomes. The accuracy and precision of the results can be assessed by analyzing reference materials and performing replicate analyses (Skoog, Holler, & Crouch, 2018).

The elemental compositions of this thesis's sample catalysts were determined using ICP-MS analysis. This analysis was performed at the Minerals Engineering Laboratory of Dalhousie University using PerkinElmer Optima 5300 DV/Optima 8300 DV equipment. Near-total acid digestion and ELTRA CS2000 with induction furnace and IR detection were employed for detecting metals. It should be noted that elements present in concentrations lower than 0.1 $\mu g \cdot g^{-1}$ (1×10^{-5} wt%) could not be detected in the catalyst samples.

3.2.5 H_2 temperature-programmed reduction (H_2-TPR)

Temperature-programmed reduction (TPR) is a commonly employed technique for analyzing metal oxides, mixed metal oxides, and metal oxides dispersed on a support. TPR provides valuable insights into the reducibility of the oxide surface and the degree of heterogeneity in reducible sites. This method enables quantitative assessment of the reduction process, offering valuable information about the surface properties of the oxide material (Skoog, Holler, & Crouch, 2018).

The fundamental concept behind reduction analysis involves detecting the variations in the 5 vol% H_2/Ar gas flow composition as it passes through the sample, compared to a reference gas with an identical composition that bypasses the sample. The total consumption of H_2 is continuously monitored using a thermal conductivity detector (TCD) and is represented as a negative signal

(which is inverted for clarity) plotted against temperature. Equation 3.14 shows the basic chemistry of the metal oxide reduction (Skoog, Holler, & Crouch, 2018).

$$M_xO_y + yH_2 \rightarrow xM + yH_2O$$

Equation 3.14

where M_xO_y is a metal oxide.

In terms of quantitative analysis, the equipment can provide the total hydrogen consumption by metal oxide species. This value is determined by integrating the total area under the TCD signal, which is recorded across the entire temperature range. Furthermore, employing a Gaussian-type deconvolution technique, the entire TPR profile can be separated into individual intermediate peaks. This allows for the determination of the relative number of different types of reducible species present in the sample. These species are identified based on the literature and their characteristic reduction temperatures (Jabbour, 2020).

In this thesis, Temperature-Programmed Reduction (TPR) experiments were performed using an NETZSCH STA 449F1 apparatus located at the Materials Engineering Department of Dalhousie University. Each TPR run utilized approximately 15 mg of the sample. Before analysis samples was purged with high-purity argon until the Thermal Conductivity Detector (TCD) baseline stabilized. Subsequently, the H_2-TPR analysis was carried out by gradually heating the samples from room temperature to 650 °C at a heating rate of 10 °C/min. Throughout the analysis, the flow rate of the 5% H_2/Ar mixture was maintained at 50 mL per minute.

3.2.6 CO_2 temperature-programmed desorption (CO_2-TPD)

Temperature-programmed desorption (TPD) is a technique used to assess the total number of active sites available for a specific probe under particular conditions, and it also reveals information about the strength distribution of these sites. The standard procedure involves introducing an excess of the probe gas to ensure coverage of all sites. Subsequently, weakly adsorbed species are

eliminated through evacuation or purging, and the probe is desorbed by heating. The desorption rate is observed as the temperature varies, either by detecting the evolved gas or monitoring the remaining species, often gravimetrically. Ammonia is commonly employed for TPD to assess acidic sites, while carbon dioxide is used for basic sites. The collected CO_2-TPD profiles are exclusively indicative of the surface of mixed metal oxides. The CO_2-TPR profile can be analyzed by deconvoluting it into Gaussian peaks, revealing the strength of the interaction between CO_2 molecules and various basic surfaces. By integrating each peak, the basic surface of the catalyst and the number of different basic sites can be evaluated (Skoog, Holler, & Crouch, 2018).

CO_2-TPD experiments were carried out using same instrument as H_2-TPR, NETZSCH STA 449F1, to analyze the properties of a fresh sample, where it underwent a reduction process. This was achieved by exposing the sample to a continuous flow of 5% H_2/Ar at a ramping rate of 5 °C/min from room temperature to 300 °C, which was then maintained for 2 hours. After reducing the sample, the reactor was cooled down to 40 °C, and the sample was saturated with pure CO_2 at 40 °C for 1 hour. To remove any unabsorbed CO_2, the sample was then flushed with Ar flow for 15 minutes. Subsequently, the reactor temperature was raised to 400 °C at a ramping rate of 5 °C/min under continuous Ar flow, while the desorbed CO_2 was detected by thermal conductivity detection (TCD). The obtained data was then used to construct a temperature-programmed desorption (TPD) graph, which provides insights into the sample's surface properties and CO_2 adsorption/desorption behavior.

3.3 Catalysts Evaluation

The catalyst assessment, which involved measuring CO_2 conversion and product selectivity, was performed using a custom-built packed bed microreactor flow system connected to online chromatography or mass spectrometry. This section outlines: i) the equipment utilized for measuring catalytic reactivity and ii) a detailed explanation of the experimental procedures involved.

3.3.1 Flow Reactor Setup

The schematic diagram of the CO_2 hydrogenation setup is presented in Figure 3.3. To evaluate the catalyst, a fixed-bed continuous flow reactor was utilized. This reactor consisted of a stainless-steel tube purchased from Swagelok Atlantic Canada, with an internal diameter of 1/4 inch and a length of 50 cm. All the necessary connections were also obtained from Swagelok Atlantic Canada; refer to Appendix A for more details on the parts.

The gas flows of H_2, CO_2, and N_2 were controlled using digital mass flow controllers (F-201CV, Bronkhorst), calibrating using a manual bubble flow meter. Pressure measurements were taken and regulated using a pressure gauge before the reactor and a back-pressure regulator (P-702CV, Bronkhorst) after the reactor. The catalyst was positioned between two layers of quartz wools within the reactor tube. To achieve an isothermal condition, the reactor was heated using a tubular furnace connected to a PID controller, ensuring that all heated components maintained the same temperature. As a precautionary measure, a filter was installed to prevent any catalyst particles from entering the analytical section. Subsequently, the products were collected and subjected to analysis using an online gas chromatograph (GC) equipped with a thermal conductivity detector (TCD) and/or a flame ionization detector (FID). To prevent liquid product condensation, all post-reactor lines and valves were heated to 140 °C. For a more detailed description of each reactor component, please refer to the supplementary section of the thesis.

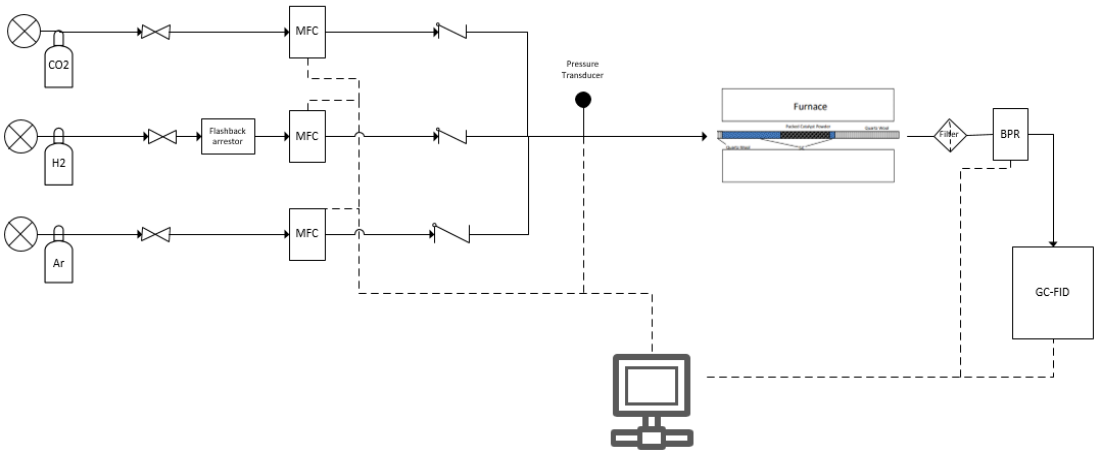

Figure 3.3: Schematic flow diagram of the microreactor system.

The sealing, safety, and thermodynamics of the high-pressure reactor system need extra consideration to achieve a safe and reliable evaluation of catalysts. Prior to constructing the system, it is crucial to assess the strength and chemical compatibility of the materials in relation to the reactants and potential products. Regular leak tests and maintenance of fitting parts and filters are essential. Furthermore, all operations involving gas feed should be conducted within a hood equipped with a hazardous gas detector. These precautions are necessary to maintain a safe working environment and mitigate any potential risks associated with the high-pressure reactor system.

3.3.2 Experimental Procedure

After loading the sample inside the reactor and before any reaction, a leak test is conducted using an inert gas like helium (He) to verify the absence of gas leakage in the system. In this procedure, a helium flow of 30 $ml.min^{-1}$ is maintained at 5 bars, and any pressure loss over 20 minutes is monitored. If a significant pressure drop occurs, indicating potential leakage (e.g., down to 1-1.5 bars), the reactor is readjusted, and the leak test is repeated until no pressure loss is observed.

3.3.2.1 Procedure

The catalysts employed for activity tests underwent crushing and sieving to obtain granules within the 40-60 mesh range. These granules were then mixed with SiC. Once the fresh catalyst sample was placed in the reactor, a purge process was conducted using a pure Ar at a flow rate of 30 $mL.min^{-1}$. The purge temperature was programmed to gradually increase from room temperature to 100 °C at a ramping rate of 2 °C/min and maintained for 30 minutes. Subsequently, the catalysts were reduced under a continuous flow of 5% H_2/Ar at a rate of 30 $mL.min^{-1}$, at a temperature of 300 °C, for 2 hours, with a ramping rate of 2 °C/min. After cooling the reactor to 180 °C, the system was pressurized with the reaction mixture, and the temperature was then elevated to the desired reaction temperature. The reaction mixture, consisting of CO_2:H_2:Ar in a ratio of 3:9:1, with a total volumetric flow rate of Y $mL.min^{-1}$, was fed into the reactor at reaction temperatures (200, 220, 240, 260 and 280 °C), under a pressure of 5 bars.

3.3.2.2 Chromatography and Mass Spectrometry

Chromatography is a method employed to analyze chemical compounds, allowing their separation and quantification in either gas or liquid samples. In the experimental setup described in this thesis, the feed stream refers to the effluent from the reactor, and analysis is conducted using a gas chromatograph (GC). This allows for the examination and quantification of the compounds in the sample. In this thesis, the Agilent MicroGC490 instrument was utilized, equipped with a thermal conductivity detector (TCD) and a flame ionization detector (FID). The chromatograph analysis software utilized in this study was provided by Agilent, namely Chemstation for the 7890A GC and EZchrom for the MicroGC490 GC. The GCs were calibrated using standard calibration gases obtained from Matheson and Sigma-Aldrich.

Mass spectrometry (MS) is a technique that employs electrons to dissociate molecules and measures the mass-to-charge ratios of the resulting fragments. Through hard ionization, the parent molecule undergoes extensive fragmentation, resulting in a fragmentation pattern that can be compared to a database (such as NIST) for identification purposes. Mass spectrometry offers

various modes of operation, allowing for the screening of potential molecules in the effluent by specifying a particular range of mass-to-charge ratios (m/z). Additionally, changes in the concentration of known molecules in the effluent can be monitored by selecting different m/z ratios. Mass spectrometry is frequently combined with gas chromatography, wherein GC facilitates separation and quantification while MS aids in compound identification. During the assessment of catalytic performance, GC typically serves as the primary method for quantifying product concentrations and selectivity. To ensure data reproducibility, catalytic measurements were repeated twice for each catalyst (Skoog, Holler, & Crouch, 2018).

The CO_2 conversion (X_{CO2}) was calculated utilizing N_2 as internal standard based on Equation 3.15.

$$X_{CO_2}(\%) = [\frac{moles\ CO_{2,out} - moles\ CO_{2,in}}{moles\ CO_{2,in}}] \times 100$$

Equation 3.15

The selectivity of product i (S_i) and space-time yield of methanol ($STY_{methanol}$) were calculated using Equation 3.16 and 3.17 respectively.

$$S_i(\%) = \frac{moles\ product_{i,out}}{\Sigma\ moles\ product_{i,out}} \times\ 100$$

Equation 3.16

$$STY_{methanol}(\frac{mmol}{g_{cat}.h}) = \frac{F_{CO_{2.in}} \times X_{CO_2}/100 \times S_{methanol}/100}{W_{cat}}$$

Equation 3.17

where $F_{CO2,\ in}$ (mmol/h) is the molar flow rate of CO_2 at the inlet of the reactor and W_{cat} (g) is the amount of catalyst.

The TOF of methanol for the Cu-based catalysts was calculated according to the number of Cu surface atoms determined by N_2O chemisorption using Equation 3.18.

$$TOF_{methanol}(\frac{molecules_{methanol}}{second.Cu_{site}}) = \frac{R_{methanol} \times N_A}{SA_{cu} \times C_M}$$

Equation 3.18

Where $R_{methanaol}$ is the methanol production rate (mol. g^{-1}. s^{-1}).

In summary, this chapter provided an overview of catalyst preparation, the characterization techniques employed in this thesis, the setup of the reactor, and the evaluation of catalysts. The subsequent chapter will delve into the results obtained from characterization and evaluation experiments, as well as provide recommendations for future research endeavors aimed at enhancing catalyst performance and advancing our understanding of CO_2 hydrogenation.

CHAPTER 4 Results and Discussions

4.1 X-Ray Diffraction (XRD)

The X-ray diffraction (XRD) patterns of the Cu/Zn/Zr/EAGs catalysts are presented in **Figure 4.1**. Notably, a diffraction peak corresponding to the (002) plane of graphite-like, indicative of amorphous EAGs, is discernible at 2θ = 25.9° degrees (PDF 00-26-1080). Consistent with expectations, the intensity of this peak exhibits a gradual increase with the rising EAG content (Zhang, et al., 2010) (Dong, Zhang, Lin, Yuan, & Tsai, 2002) (Liang, Dong, Lin, & Zhang, 2009) (Wang, et al., 2015) (Sun, et al., 2018).

The peaks observed at 35.6°, 38.9°, and 48.6° corresponding to the (002), (111), and (202) diffraction planes of the catalyst were characteristic of crystalline CuO (PDF 00- 045-0937). These CuO species can form during the ageing or drying of the precursors (Stangeland, 2021).

The diffraction lines observed at 2θ values of 31.7°, 56.3°, 62.9°, and 68.0° correspond to the ZnO crystal structure (PDF-00-065-0726). Furthermore, the peaks within the ranges of (30.1-34.2°) and (56.9-58.4°), as well as the peak at 60.8°, can be attributed to the tetragonal zirconia phase (PDF-00-049-1746). The weak and broad ZnO and ZrO_2 peaks observed here signify the presence of amorphous, dispersed, and intricately intertwined metal oxide particles. This finding aligns with previous literature, showing that Zn and Zr tend to exhibit apparent crystallization only after calcination at temperatures exceeding 500 degrees Celsius (Wang, et al., 2015).

Notably, the diffraction peaks associated with metal oxides, especially CuO, become stronger and more pronounced with the addition of higher amounts of EAGs, in contrast to lower levels of EAG incorporation.

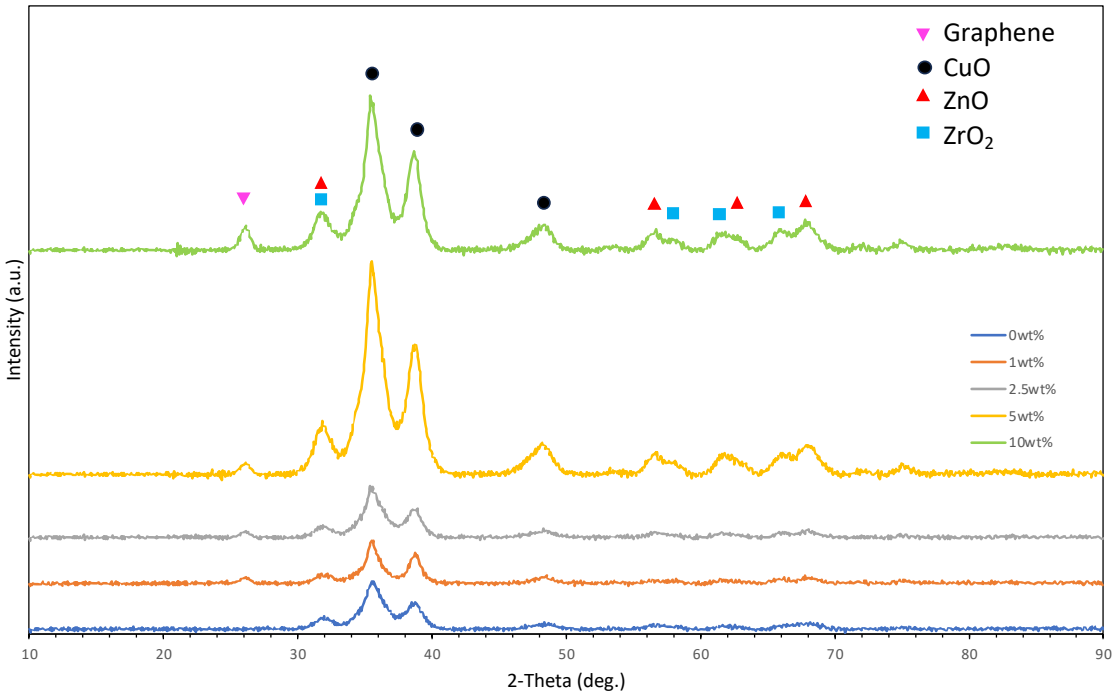

Figure 4.1: XRD patterns of Cu/Zn/Zr/EAGs catalysts.

The enhancement of peak intensity and sharpness generally implies larger crystal sizes, which may not be conducive to hydrogen (H_2) absorption. Several studies have proposed that dispersed and smaller Cu particles exhibit a higher rate of H_2 absorption (Li & Chen, 2019) (Sun, et al., 2018) (Wang, et al., 2015). This observation has been elucidated in the existing literature, which suggests that a higher percentage of EAG results in the aggregation of metal oxides (Witoon, et al., 2018). Despite examining the catalyst samples without grinding or any additional treatment, it is essential to acknowledge the potential impact of strain-induced peak broadening on the observed crystallite size. The average crystal size of CuO particles was determined employing the Scherrer equation, yielding values of 5.28, 4.97, 4.68, 5.66, and 5.93 nm for Cu/Zn/Zr/EAGs (P1, P2, P3, P4, P5) catalysts, respectively. Therefore, it can be concluded that proper incorporation of a minor amount of the EAGs into significantly decrease Cu particle size, generating more catalytically active Cu sites at the catalyst surface for CO/CO_2 hydrogenation reaction (Dong, Zhang, Lin, Yuan, & Tsai, 2002). While it is recognized that the process of CuO reduction may induce reorganization and coalescence of metallic copper atoms, leading to the formation of larger Cu crystallites, the data

acquired herein offers valuable insights into the impact of carbon nanotube incorporation on the size of metal oxide particles.

4.2 N_2 physisorption

The investigation of the BET surface area, pore volume, and average pore diameter of the catalysts was conducted through meticulous N_2 adsorption analysis, and the ensuing findings are presented in Table 4.1.

Table 4.1: Surface Properties Analysis of Cu/Zn/Zr/EAGs Catalysts: BET Surface Area, Pore Volume, and Pore Diameter Measurements

Samples	Specific surface area (m^2/g)	Pore volume Data (cc/g)	Pore Size Radius (nm)
Cu/Zn/Zr/EAGs-P1	79.44	0.03304	1.838
Cu/Zn/Zr/EAGs-P2	87.1293	0.03357	1.839
Cu/Zn/Zr/EAGs-P3	90.8396	0.0352	1.838
Cu/Zn/Zr/EAGs-P4	77.44	0.03195	1.837
Cu/Zn/Zr/EAGs-P5	75.89	0.03137	1.838

BET-specific surface area results reveal that introducing a minor quantity of EAG has led to a significant augmentation in the specific surface area. Specifically, a notable 10% and 14% increase was observed for the Cu/Zn/Zr/EAGs-P2 and Cu/Zn/Zr/EAGs-P3 catalysts when compared to the Cu/Zn/Zr/EAGs-P1 counterpart. However, it is worth noting that a higher loading of EAGs results in a sudden decline in the specific surface area. A similar pattern was observed in the case of catalysts with graphene oxide additives (Witoon, et al., 2018). This trend can be attributed to the tendency of EAGs to re-stack at higher loadings, leading to the aggregation of metal and metal oxide particles. As previously mentioned, the specific surface area is a pivotal characteristic of catalysts, crucial for predicting their performance. It is widely recognized that a greater specific

surface area leads to an increase in active sites, consequently enhancing overall performance (Li & Chen, 2019).

These outcomes consistently correlate with the results obtained from the H_2-TPD tests, which will be discussed later in this study. Furthermore, a comparable trend in specific surface area was also observed in the data on pore volume, with the catalysts categorized as P3 > P2> P1 > P4 > P5 EAGs. Notably, the pore size radius and isotherm type remained consistent among all catalyst variants examined in this study.

4.3 Scanning electron microscopy (SEM):

Scanning electron microscopy (SEM) has been employed as a crucial tool to gain insights into the EAGs and its impact on catalysts, offering a detailed examination of their morphologies. **Figure 4.2** and

Figure 4.3 comprehensively compares the discernible morphological characteristics of both pristine EAGs and functionalized EAGs (F-EAGs) at two distinct scales, 5 and 100 µm.

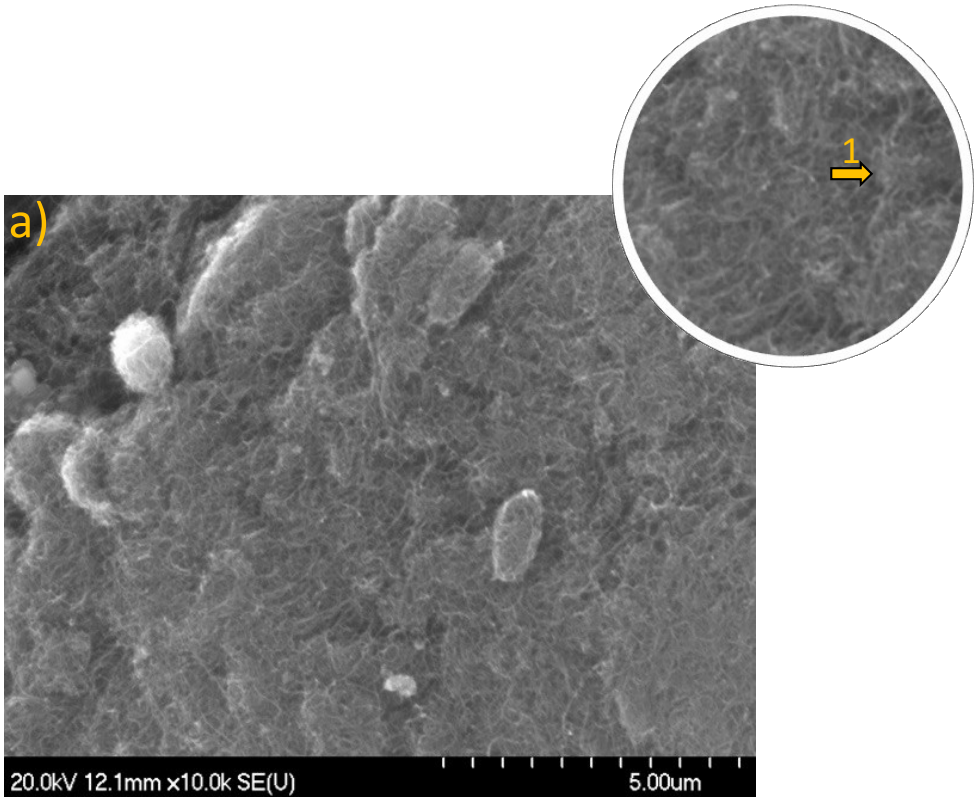

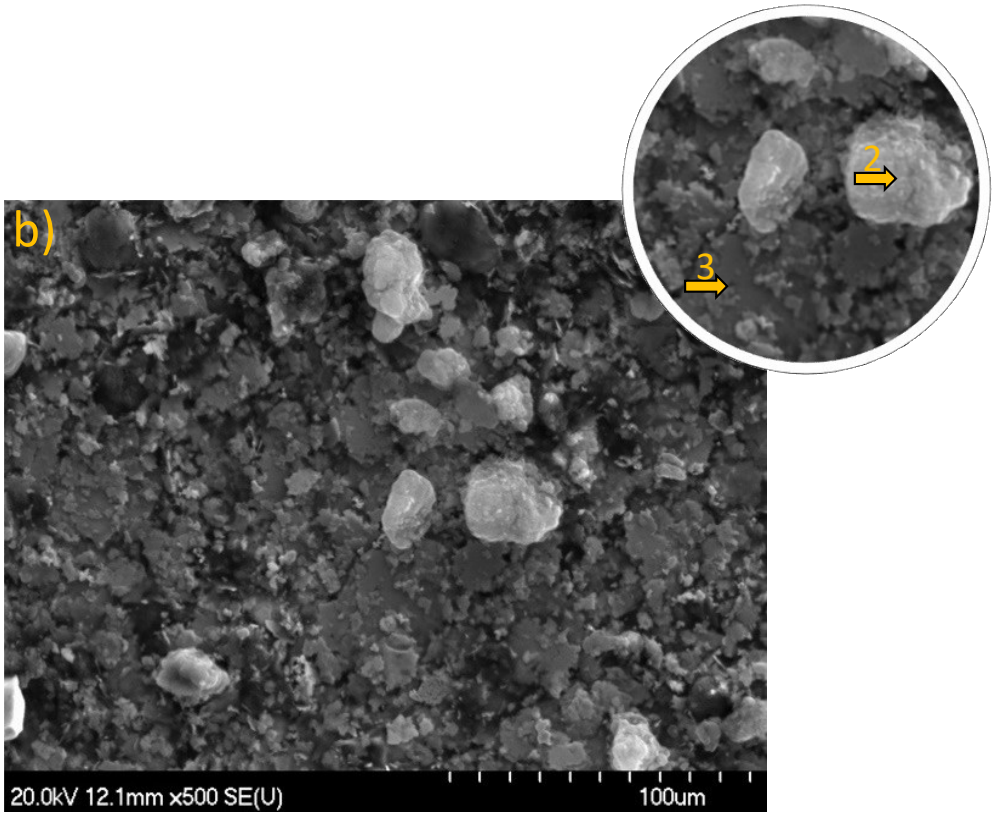

1) EAG
2) EAG grain
3) Silver coating

Figure 4.2: SEM images of EAGs surface at a) 5 µm and b) 100 µm

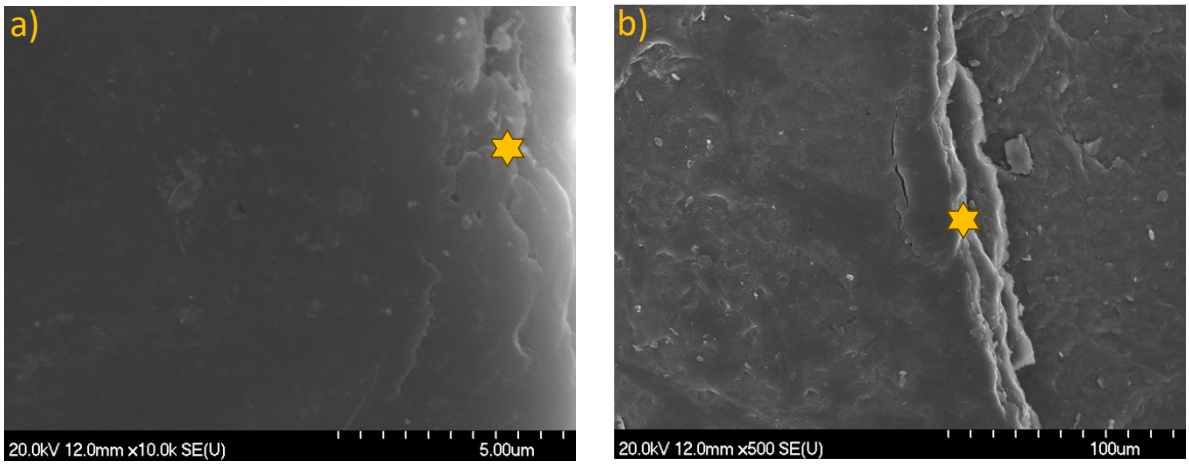

* F-EAGs paste cracks

Figure 4.3: SEM images of F-EAGs surface at a) 5 µm and b) 100 µm

The SEM examination of EAGs at 100 μm reveals a characteristic EAG grain structure. However, at a smaller scale of 5 micrometres, the morphologies exhibit the expected features of wrinkled, entangled, and EAGs.

In contrast, Functionalized EAGs (F-EAGs) morphologies at 100 μm predominantly comprises a uniform layer of dark paste. Remarkably, even at the smaller scale of 5 μm, the morphological analysis reveals and extremely densely packed structure. Despite the primary objective of functionalization being the enhancement of EAGs' solubility and their conversion into open-ended structures for improved catalyst synthesis, the results demonstrate an intriguing phenomenon. Functionalization not only rendered the EAGs soluble but also facilitated the alignment of densely packed EAGs, forming a paste-like structure (Rosca, Watari, Uo, & Akasaka). This underscores the exceptional effectiveness of the functionalization process in achieving a high degree of alignment and uniformity in the EAGs, a critical factor in optimizing their catalytic properties (Großmann, 2013)).

Figure 4.4, shows the apparent morphologies of the catalyst samples at 5 μm. Notably, a distinct transformation in the morphology is observed when comparing EAGs-free catalysts (Figure 4.4 (a)), with their EAGs-containing counterparts (Figure 4.4 (b-e)). The Cu/Zn/Zr/EAGs-P1 catalyst exhibits a composition characterized by block-structured/tetragonal-shaped particles with minimal porosity and a uniform surface. The introduction of even a small quantity of EAGs into the catalyst induces a perceptible shift in surface structure, resulting in a more cloud-like, homogeneous, and amorphous configuration. Interestingly, the presence of EAGs is conspicuous even in the Cu/Zn/Zr/EAGs-P2 sample.

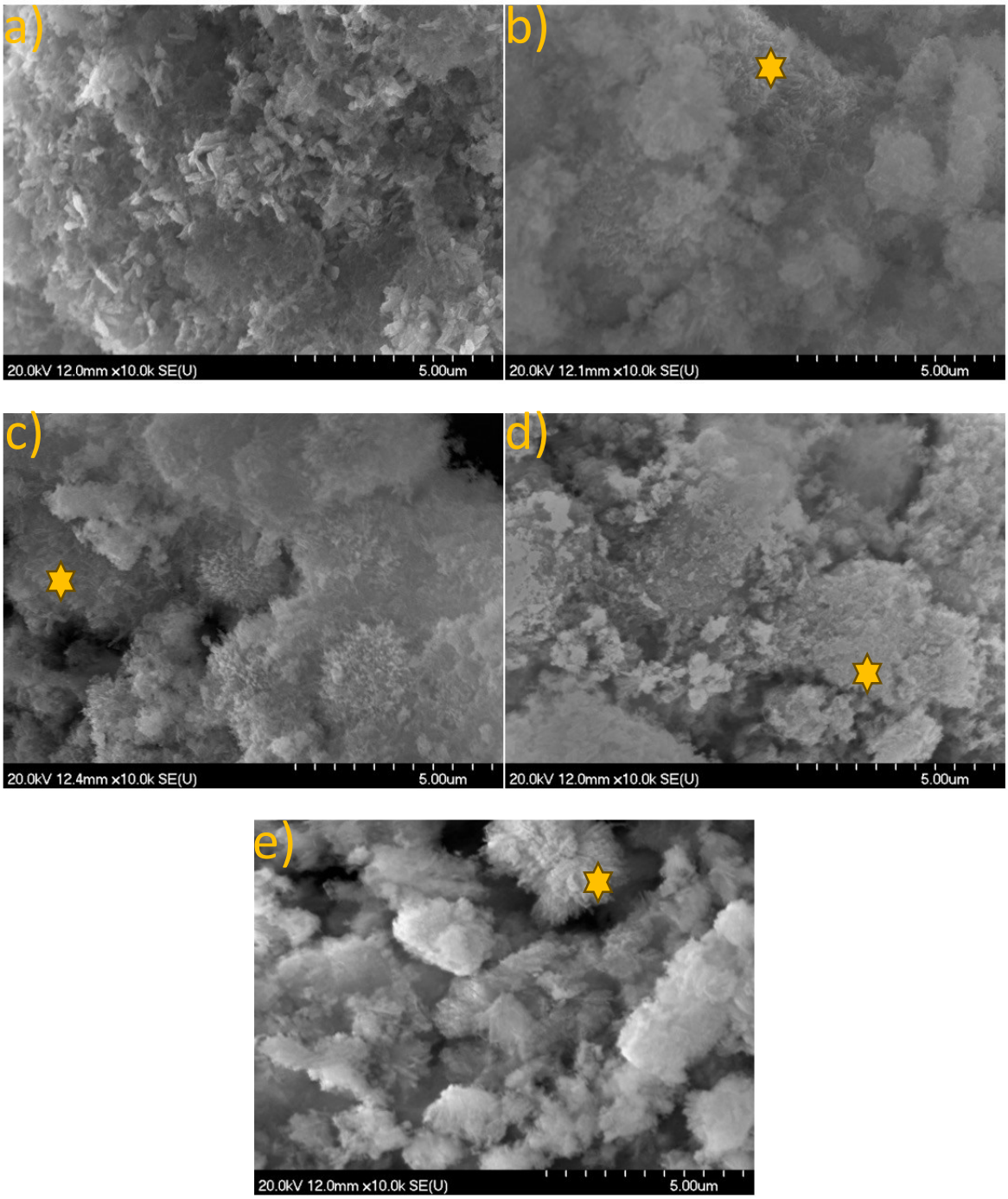

* EAG

Figure 4.4: SEM images of (a) Cu/Zn/Zr/EAGs-P1 (b) Cu/Zn/Zr/EAGs-P2 (c) Cu/Zn/Zr/EAGs-P3 (d) Cu/Zn/Zr/EAGs-P4 (e) Cu/Zn/Zr/EAGs-P5 surface at 5 μm.

An increase in the EAGs content within the catalyst results in a higher degree of irregularity in particle shapes and greater particle density. Catalysts containing high amounts EAGs exhibit a wide range of particle sizes and clustering, attributed to the distribution of EAGs within the structure and metal/metal oxide agglomeration (Fan & Wu, 2016) (Witoon, et al., 2018).

This SEM analysis provides valuable insights into the evolving morphologies of catalysts as a function of EAGs content, shedding light on the structural changes associated with incorporating EAGs.

4.4 Inductively Coupled Plasma Mass Spectrometry (ICP-MS)

The ICP-AES analysis results detailing the nominal and actual composition of metal and metal oxide catalysts have been presented in Table 4.2.

Table 4.2: ICP-AES results of Cu/Zn/Zr/EAGs Catalysts

ICP	**Percentage**		
Samples	Cu	Zn	Zr
Nominal Target	60.00%	30.00%	10.00%
Cu/Zn/Zr/EAGs-P1	63.49%	29.08%	7.43%
Cu/Zn/Zr/EAGs-P2	62.60%	29.92%	7.47%
Cu/Zn/Zr/EAGs-P3	64.22%	29.86%	5.92%
Cu/Zn/Zr/EAGs-P4	65.24%	30.22%	4.54%
Cu/Zn/Zr/EAGs-P5	63.35%	28.60%	8.05%

The metal content in the catalysts closely approximates the targeted nominal values of 60%, 30%, and 10% for Cu, Zn, and Zr, respectively. Notably, the Zr content in catalysts synthesized through the co-precipitation method consistently falls below the nominal values. This phenomenon underscores a common challenge associated with co-precipitation procedures, wherein precise control over elemental compositions is elusive. The variations in pH levels during the procedure

give rise to deviations from the intended ratios of desired metals, mainly when dealing with compounds characterized by high solubility product values (Stangeland, 2021) (Gao, 2021).

While ICP serves as a robust analytical technique primarily designed for elemental analysis, specifically for quantifying the concentrations of metallic and non-metallic elements within a sample, it is noteworthy that its applicability in detecting carbonaceous materials within metal or metal oxide catalysts remains somewhat limited. These limitations encompass challenges related to carbon detection, carbon ionization, and matrix effects. Consequently, the decision has been made to restrict the use of ICP solely to assess metal-to-metal oxide ratios within the catalyst systems under investigation, recognizing its unsuitability for comprehensive carbon-related analyses (Gao, 2021) (Großmann, 2013).

4.5 H_2 temperature-programmed reduction (H_2-TPR)

The reducibility of catalysts was thoroughly investigated through H_2-temperature-programmed reduction (H_2-TPR), and the resulting profiles are thoughtfully depicted in **Figure 4.5**. These profiles were acquired over a temperature range spanning from 100 to 300°C, offering valuable insights into the reduction of hydrogen species on the catalysts under examination.

In accordance with existing literature, the profile peaks can be classified into two primary categories: those occurring at lower temperatures and those manifesting at higher temperatures. The lower-temperature reductions, typically observed in the range of 100–150°C, can be attributed to the reduction of amorphous or highly dispersed CuO species or the conversion of CuO to Cu_2O and, eventually, the formation of metallic copper species through gradual reduction processes. Conversely, the high-temperature reductions, typically occurring above 150°C, can be ascribed to the reduction of bulk-like CuO entities. Importantly, no discernible reduction of other metals was observed in these experiments (Águila, et al., 2009) (Wang, et al., 2015) (Sun, et al., 2018). Significantly, the positioning of these reduction peaks can serve as a determinant of particle sizes, with lower temperature peaks favouring smaller copper particle sizes, a phenomenon recognized to enhance hydrogen adsorption capacity. Furthermore, a lower reduction temperature peak is theoretically conducive to restraining the growth of metal Cu crystallites formed during H_2

reduction. Consequently, it is advantageous for increasing the exposed Cu surface area, thereby augmenting catalyst activity (Wang, et al., 2015).

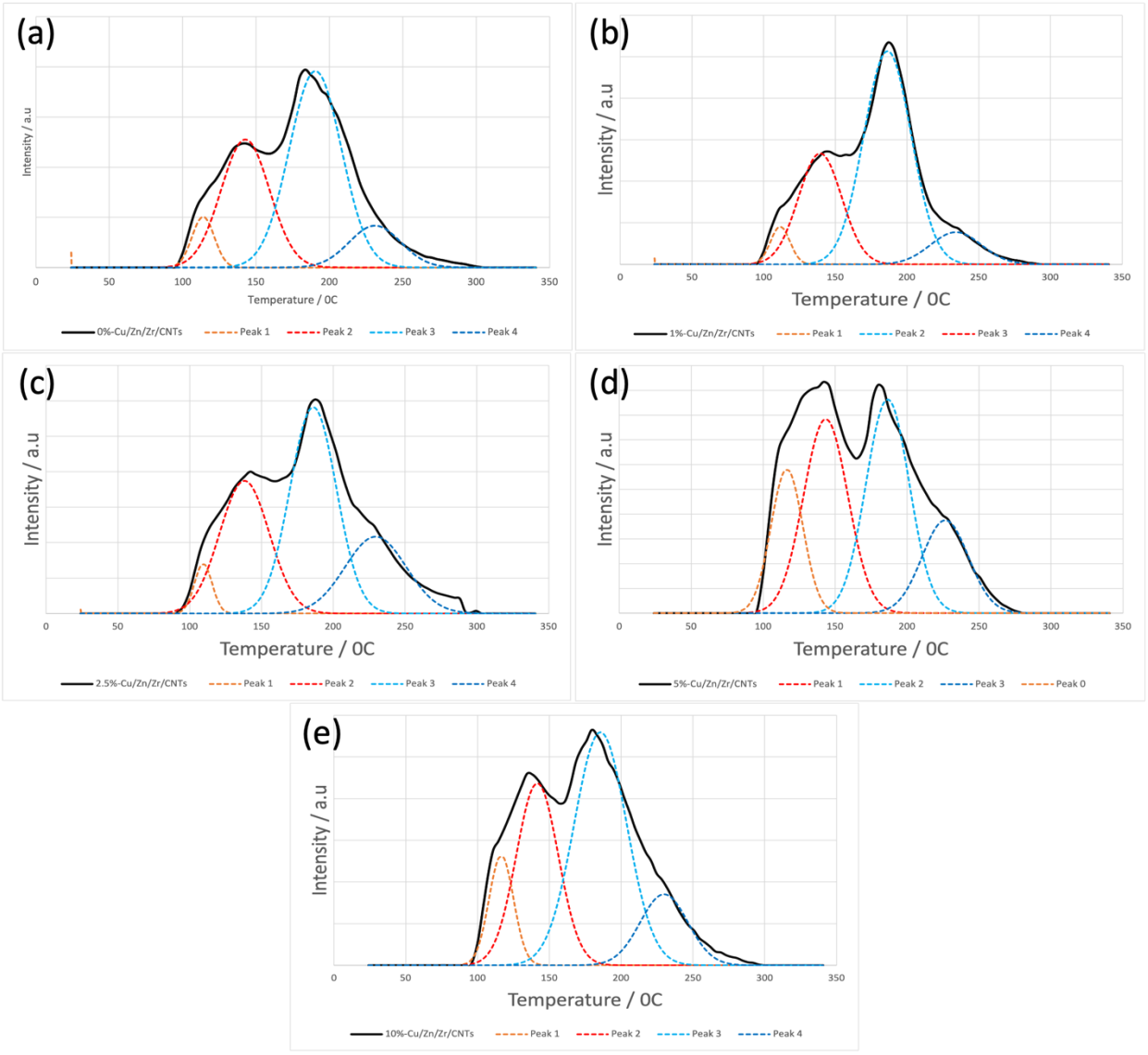

Figure 4.5: H_2-TPR profiles with the deconvolution of (a) Cu/Zn/Zr/EAGs-P1 (b) Cu/Zn/Zr/EAGs-P2 (c) Cu/Zn/Zr/EAGs-P3 (d) Cu/Zn/Zr/EAGs-P4 (e) Cu/Zn/Zr/EAGs-P5

As Figure 4.5 and Table 4.3 show, including a small amount of EAGs in the catalysts has the most effect on the positions of the reduction peaks. The incorporation of low amount of EAGs leads to a downward shift in the position of the low-temperature maxima peak, while a slightly higher percent inclusion results in a shift in the position of all peaks. Intriguingly, the addition of a higher

concentration of EAGs has minimal to no effect on the position of the temperature maxima peak, and in certain instances, it even causes an elevation in position for specific peaks. It is worth highlighting that the catalyst Cu/Zn/Zr/EAGs-P3 shows the lowest temperature peak position among all the EAG-containing catalysts and even for non-containing catalyst.

However, it's crucial to emphasize that the interaction between copper oxide and the carrier significantly influences the reduction properties of copper-based catalysts. The intensity of the lower temperature peaks exhibits substantial variations with the addition of EAGs. The graphical representation reveals that the intensity of the lower temperature peaks increases upon the addition of small quantities of EAGs, specifically Cu/Zn/Zr/EAGs-P2 and Cu/Zn/Zr/EAGs-P3 However, an increase in EAG content beyond these percentages results in a reduction not only in lower-temperature hydrogen intake but also in higher-temperature reductions. The quantification of hydrogen consumption at various reduction stages was achieved by applying the Gaussian function on TPR curve fitting.

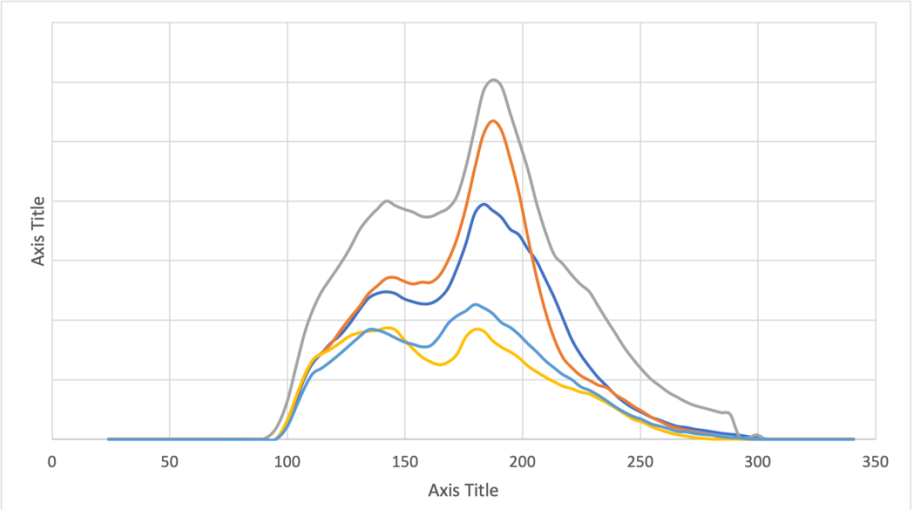

Figure 4.6: H_2-TPR profiles of Cu/Zn/Zr/EAGs catalysts.

Table 4.3: H_2-TPR data of Cu/Zn/Zr/EAGs catalysts.

Catalysts	T_{M1}[a]	T_{M2}[a]	T_{M3}[a]	T_{M4}[a]	Low Temps Relative Intensity[b]	Total Relative Intensity[c]
Cu/Zn/Zr/EAGs-P1	114	143	190	231	1.00	1.00

Cu/Zn/Zr/EAGs-P2	112	139	186	234	1.09	1.08
Cu/Zn/Zr/EAGs-P3	109	138	186	229	1.47	1.60
Cu/Zn/Zr/EAGs-P4	116	143	186	226	0.74	0.56
Cu/Zn/Zr/EAGs-P5	116	142	186	230	0.69	0.65

[a] Temperature of the peak maxima.
[b] Sum of Low-temperature peaks areas relative to Cu/Zn/Zr/EAGs-P1.
c Sum of all peaks area relative to Cu/Zn/Zr/EAGs-P1.

The Cu/Zn/Zr/EAGs-P3 catalyst demonstrates a significant enhancement in hydrogen absorption, with 1.47 times greater absorption at lower temperatures and a remarkable 60 precents increase in overall absorption compared to non-EAG-containing catalyst.

Overall, the sequence of hydrogen reduction rates follows the trend of P3> P1 > P2 > P4 > P5 EAGs. This indicates that introducing a small amount of EAGs can stimulate the reduction process, while higher EAG concentrations tend to lead to copper crystallization. Interestingly, these findings align with similar experiments conducted using graphene oxide as an additive in catalyst formulations (Witoon, et al., 2018). It is believed that EAGs serve as an excellent adsorbent, activator, and reservoir of H_2, which would be beneficial to generating microenvironments with a higher stationary-state concentration of active hydrogen on the surface of the catalyst, and thus favourable to enhancing the rate of the CO/CO_2 hydrogenation reactions (Dong, Zhang, Lin, Yuan, & Tsai, 2002).

These findings shed light on the intricate interplay between EAGs and copper-based catalysts during the reduction process, offering valuable insights for optimizing catalyst performance in hydrogen-related applications.

4.6 CO_2 temperature-programmed desorption (CO_2-TPD)

The effect of incorporating EAGs into the CZZ system on the adsorption of carbon dioxide (CO_2) was evaluated using CO_2 Temperature-Programmed Desorption (CO_2-TPD).

The resulting CO_2-TPD profiles, as illustrated in **Figure 4.7**, were obtained across a temperature range spanning from 40 to 400°C, thereby providing valuable insights into various aspects of CO_2 adsorption, including the identification of adsorption sites, their quantification, and the correlation

between metal and metal oxide particles. In accordance with established literature, the observed CO_2-TPD profile peaks can be deconvoluted into three Gaussian distributions, each corresponding to distinct classes of basic adsorption sites, namely weakly basic (WB), moderately basic (MB), and strongly basic (SB) sites (Witoon, et al., 2018) (Stangeland, 2021). These sites can be ascribed as follows:

- Weakly basic sites are primarily attributed to surface hydroxyl groups, denoted as ZnOH and ZrOH. These surface hydroxyl groups exhibit relatively lower basicity compared to the other sites and mostly favour CO formation.
- Moderately basic sites are associated with metal-oxygen pairs, specifically ZnO and ZrO. These sites possess a moderate level of basicity and play a significant role in CO_2 adsorption and catalyst selectivity.
- Strongly basic sites can be attributed to low coordination oxygen atoms. These highly basic sites represent the most active and effective CO_2 adsorption sites.

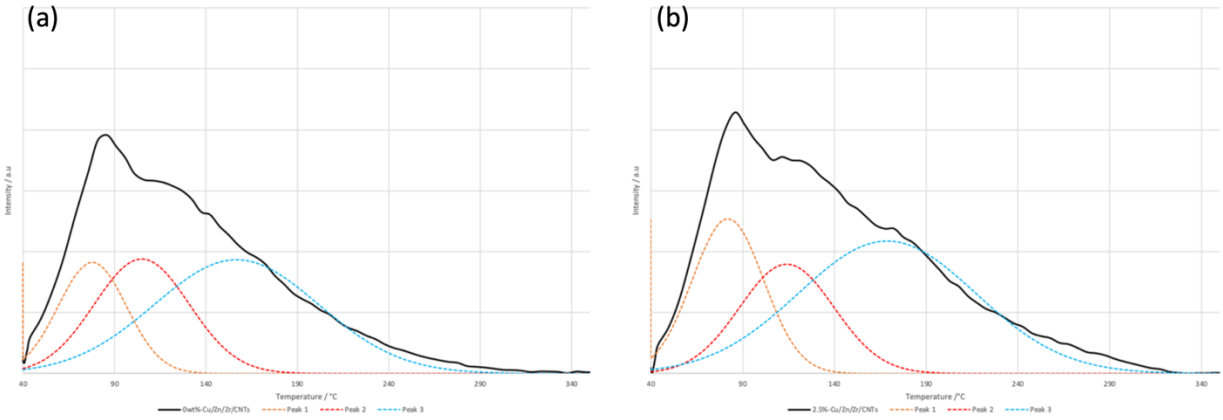

Figure 4.7: CO_2-TPD profiles with the deconvolution of (a) Cu/ZN/Zr/EAGs-P1 (b) Cu/ZN/Zr/EAGs-P3

As there is no CO_2 thermal desorption signal over the bare EAGs under the condition investigated (Yu, et al., 2013), the CO_2-TPD profiles collected exclusively indicate mixed metal oxide surfaces. Furthermore, it is noteworthy that three distinct categories of adsorbed CO_2 species, specifically

bicarbonate species, bidentate carbonates, and unidentate carbonates, were identified as forming on these three distinct types of surface basic sites, respectively (Gao, et al., 2013).

As summarized in Table 4.4, The EAGs-free catalyst shows the desorption peak at 78, 105 and 157 °C for weakly, moderately, and strongly basic sites, respectively. The incorporation of EAGs significantly shifts the desorption peak to higher temperatures, 82, 114, and 169 °C, respectively, boosting the strength between CO_2 molecules and the surface of the catalysts.

The addition of a modest quantity of EAGs yields a noteworthy augmentation in the abundance of basic sites. This substantial enhancement, equivalent to a 21 percent increase in total CO_2 absorption, unequivocally signifies an improved CO_2 absorption capacity. Remarkably, the combined quantity of moderately and strongly basic sites increases by 14 percent, implying an augmented number of interfacial contacts between metal/metal oxides which can likely be attributed to the reduced size of metal oxide crystallites as seen in XRD. Moreover, it is stated in other publications that the combination of copper and zinc precursors with carbonate salt leads to the creation of Cu-Zn hydroxycarbonate entities. Subsequently, upon calcination, this process facilitates the establishment of close proximity between the CuO and ZnO surfaces (Fujitani, Nakamura, Ueno, Uchijima, & Nakamura, 1997).

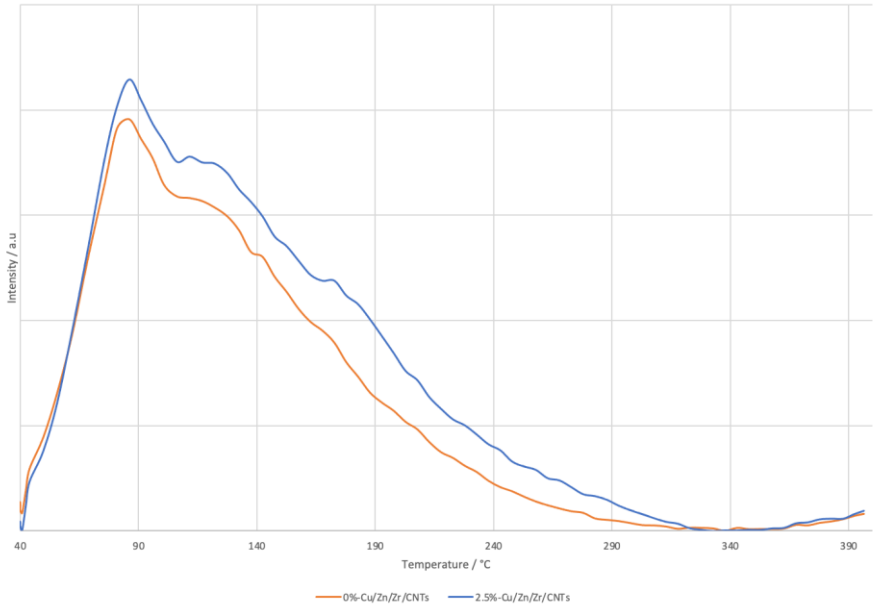

Figure 4.8: CO_2-TPD profiles of Cu/ZN/Zr/EAGs-P1 and Cu/ZN/Zr/EAGs-P3.

Table 4.4: CO_2-TPD data of Cu/Zn/Zr/EAGs catalysts

Catalysts	T_{WB}[a]	T_{MB}[a]	T_{SB}[a]	(MB+SB) Relative Intensity[b]	Total Relative Intensity[c]
Cu/Zn/Zr/EAGs-P1	78	105	157	1.00	1.00
Cu/Zn/Zr/EAGs-P3	82	114	169	1.14	1.21

[a] Temperature of the peak maxima.
[b] Sum of MB and SB peak areas relative to Cu/Zn/Zr/EAGs-P1.
c Sum of all peaks area relative to Cu/Zn/Zr/EAGs-P1.

Although CO_2 conversion depends on the exposed Cu surface area, the CH_3OH selectivity is known to increase linearly with the proportion of strongly basic sites to the total basic sites (Witoon, et al., 2018). Notably, the percentage of strongly basic sites to the total basic sites has exhibited an increase from 51 percent in the EAGs-free catalyst to 53 percent for Cu/ZN/Zr/EAGs-P3 catalyst. This outcome suggests that factors beyond the BET surface area must contribute to the increase in the count of strongly basic sites, as the density of basic sites would remain constant if the sole determinant were the BET surface area (Gao, et al., 2013). Consequently, it can be inferred that the incorporation of EAGs leads to an augmentation in the exposed surface area of ZrO_2.

These discoveries illuminate the complex interplay between EAGs and metal oxides in the context of the CO_2 absorption process, providing valuable insights that can aid in the optimization of catalyst performance for applications related to hydrogen.

CHAPTER 5 Conclusion

5.1 Conclusions

In conclusion, this master's thesis has presented a comprehensive investigation into the impact of EAG incorporation on Cu/Zn/Zr-based catalysts for CO/CO_2 hydrogenation reactions. The study's findings have been derived from a combination of analytical techniques, including X-ray diffraction (XRD), BET surface area analysis, scanning electron microscopy (SEM), ICP-AES analysis, H_2-temperature-programmed reduction (H_2-TPR) and CO_2-temperature-programmed desorption (CO_2-TPD), shedding light on the structural, morphological, and reducibility aspects of these catalysts. The key results and their implications are summarized below:

- The XRD patterns revealed that the introduction of EAGs led to changes in the crystallinity and peak intensities of metal oxides, especially CuO. The Scherrer equation was applied to determine the average crystal size of CuO particles in the catalysts. It was found that the proper incorporation of a minor amount of EAGs resulted in a significant decrease in Cu particle size, potentially leading to the generation of more catalytically active Cu sites for CO/CO_2 hydrogenation.

- The BET surface area analysis showed that a low quantity of EAGs (Cu/ZN/Zr/EAGs-P2 and Cu/ZN/Zr/EAGs-P3) led to a significant increase in the specific surface area, which is crucial for enhancing catalytic performance. However, higher EAG loadings caused a decline in the specific surface area due to EAG distribution and metal/metal oxides agglomeration.

- SEM images revealed the morphological changes in the catalysts as a function of EAG content. The introduction of EAGs led to a shift from block-structured/tetragonal-shaped particles with minimal porosity and a uniform surface to more cloud-like, amorphous structures with higher EAG content, indicating agglomeration and structural changes in the catalysts. Catalysts containing higher EAGs exhibit a wide range of particle sizes and

clustering, attributed to the redistribution of EAGs within the structure and metal/metal oxides agglomeration. The alignment and uniformity of EAGs in the functionalized form were also highlighted, emphasizing their role in optimizing catalytic properties.

- The ICP-AES analysis confirmed that the metal content in the catalysts closely matched the targeted nominal values.

- H_2-TPR profiles demonstrated that the addition of EAGs influenced the reduction peaks' positions and intensities. A low amount of EAGs (Cu/ZN/Zr/EAGs-P2 and Cu/ZN/Zr/EAGs-P3) stimulated the reduction process, resulting in lower temperature peaks favoring smaller copper particle sizes and higher hydrogen absorption. Higher EAG concentrations led to copper crystallization, reducing both lower and higher temperature reductions.

- CO_2-TPD profiles demonstrated that the addition of EAGs influenced the CO_2 desorption peaks' positions and intensities. A low amount of EAGs (Cu/ZN/Zr/EAGs-P3) stimulated the desorption process, resulting in higher temperature peaks and increasing total CO_2 desorption by 1.21-fold, favoring more selective methanol production.

In summary, the incorporation of EAGs into Cu/Zn/Zr catalysts for CO/CO_2 hydrogenation reactions had a profound impact on their structure, surface properties, and reduction behavior. Small quantities of EAGs, especially Cu/ZN/Zr/EAGs-P3 were found to enhance surface area, reduce Cu particle size, and promote hydrogen and carbon dioxide adsorption, ultimately improving the catalyst's performance. However, higher EAG loadings led to agglomeration and reduced catalytic activity. These findings contribute to a deeper understanding of the interplay between EAGs and copper-based catalysts, offering insights for optimizing catalysts in hydrogen-related applications. Further research is warranted to explore the full potential of EAGs as catalyst modifiers and to optimize EAG loading for maximum catalytic efficiency.

5.2 Recommendations

Instrument Selection for Precise Analysis: Employing Micromeritics equipment for H_2-TPR and CO_2-TPD experiments is recommended due to its simplicity, accuracy, and reproducibility advantages. Using specialized equipment like Micromeritics ensures that experimental conditions are tightly controlled, leading to more reliable and consistent results in studying catalyst properties.

Enhancing Catalyst Characterization Through N_2O-Chemisorption: In addition to performed tests, it is recommended as a valuable complementary technique. This test precisely measures key catalyst properties, including Cu surface area, Cu dispersion, and Cu crystallite size. These data are essential for a comprehensive characterization of the catalysts and can be further utilized to calculate the copper turnover frequency, a critical parameter in assessing catalytic activity and efficiency. For further information on N_2O-Chemisorption, refer to the abstract.

5.3 Future Works

In the Cu-based catalysts containing EAGs, there remains substantial untapped potential for enhancing both catalytic activity and selectivity. This potential hinges on optimizing crucial factors, including the interactions between Cu, metal oxide, and EAGs. A comprehensive exploration of the active sites and the intricate interplay among active constituents, promoters, and the support matrix is imperative for fine-tuning the distinct catalytic phases. Consequently, pioneering innovative synthesis methodologies that target the optimization of Cu, metal oxide and EAG interactions individually necessitates further in-depth investigation.

In this context, the utilization of a wet-impregnation method in catalyst development, coupled with an augmented EAG loading, holds promise for pushing the boundaries of catalyst performance. Notably, even though an increased EAG content did not yield discernible improvements in catalyst efficiency, it remains plausible that higher EAG proportions could yield enhanced stability, thereby warranting further exploration in this direction.

To further enhance our understanding of the incorporation of EAGs and their impact on metal/metal oxide interactions, it is essential to conduct CO_2-TPD tests for remaining catalyst samples. The reactor's components have been successfully ordered, and most of the parts have already arrived. In the upcoming phase of this project, our focus will shift towards the assembly of the reactor, followed by a critical reactivity test. While it may be surprising that the catalyst selection could yield such divergent results as those obtained from H_2-TPR and CO_2-TPD analyses, the forthcoming reactivity test promises to provide precise measurements, enabling a meaningful comparison between our catalysts and their industrial counterparts. Additionally, it is imperative to conduct a stability test to emphasize the advantages of incorporating EAGs into the catalyst system.

References

Águila, G., Jiménez, J., Guerrero, S., Gracia, F., Chornik, B., Quinteros, S., & Araya, P. (2009). A novel method for preparing high surface area copper zirconia catalysts. Influence of the preparation variables. *Applied Catalysis*, 98–105.

Álvarez, A., Bansode, A., Urakawa, A., Bavykina, A. V., Wezendonk, T. A., Makkee, M., . . . Kapteijn, F. (2017). Challenges in the Greener Production of Formates/Formic Acid, Methanol, and DME by Heterogeneously Catalyzed CO2 Hydrogenation Processes. *Chemical reviews*, 9804-9838.

Abbas, I., Kim, H., Shin, C.-H., Yoon, S., & Jung, K.-D. (2019). Differences in bifunctionality of ZnO and ZrO2 in Cu/ZnO/ZrO2/Al2O3 catalysts in hydrogenation of carbon oxides for methanol synthesis. *Applied catalysis. B, Environmental*, 117971.

Agarwal, A. K. (2019). *Methanol and the Alternate Fuel Economy.* Springer Singapore.

Amenomiya, Y. (1987). Methanol synthesis from CO2 + H2 II. Copper-based binary and ternary catalysts Amenomiya, Y. *Applied catalysis*, 57-68.

Andersson, K. a. (2015). *Methanol as a marine fuel report.* FCBI Energy.

Arena, F., Barbera, K., Italiano, G., Bonura, G., Spadaro, L., & Frusteri, F. (2007). Synthesis, characterization and activity pattern of Cu-ZnO/ZrO2 catalysts in the hydrogenation of carbon dioxide to methanol. *Journal of catalysis*, 185-194.

Arena, F., Italiano, G., Barbera, K., Bordiga, S., Bonura, G., Spadaro, L., & Frusteri, F. (2008). Solid-state interactions, adsorption sites and functionality of Cu-ZnO/ZrO2 catalysts in the CO2 hydrogenation to CH3OH. *Applied catalysis. A, General*, 16-23.

Arena, F., Mezzatesta, G., Zafarana, G., Trunfio, G., Frusteri, F., & Spadaro, L. (2013). Effects of oxide carriers on surface functionality and process performance of the Cu–ZnO system in the synthesis of methanol via CO2 hydrogenation. *Journal of catalysis*, 141-151.

Arena, F., Mezzatesta, G., Zafarana, G., Trunfio, G., Frusteri, F., & Spadaro, L. (2013). How oxide carriers control the catalytic functionality of the Cu–ZnO system in the hydrogenation of CO2 to methanol. *Catalysis today*, 39-46.

Baltes, C., Vukojević, S., & Schüth, F. (2008). Correlations between synthesis, precursor, and catalyst structure and activity of a large set of CuO/ZnO/Al2O3 catalysts for methanol synthesis. *Journal of Catalysis*, 334-344.

Barrett, E. P., Joyner, L. G., & Halenda, P. P. (1951). The Determination of Pore Volume and Area Distributions in Porous Substances. I. Computations from Nitrogen Isotherms. *Journal of the American Chemical Society*, 373-380.

Bartholomew, C., & Farrauto, R. (2011). *Fundamentals of industrial catalytic processes.* John Wiley & Sons.

Basile, A., & Dalena, F. (2018). *Methanol - Science and Engineering.* Elsevier Science & Technology Books.

Behrens, M., Furche, A., Kasatkin, I., Trunschke, A., Busser, W., Muhler, M., . . . Schlögl, R. (2010). The Potential of Microstructural Optimization in Metal/Oxide Catalysts: Higher Intrinsic Activity of Copper by Partial Embedding of Copper Nanoparticles. *ChemCatChem*, 816-818.

Behrens, M., Studt, F., Tovar, M., Fischer, R. W., Norskov, J. K., Schlogl, R., . . . Benjamin-Lou, K. (2012). The Active Site of Methanol Synthesis over Cu/ZnO/Al2O3 Industrial Catalysts. *Science (American Association for the Advancement of Science)*, 893-897.

Bonura, G., Arena, F., Mezzatesta, G., Cannilla, C., Spadaro, L., & Frusteri, F. (2011). Role of the ceria promoter and carrier on the functionality of Cu-based catalysts in the CO_2-to-methanol hydrogenation reaction. *Catalysis today*, 251-256.

Bonura, G., Cordaro, M., Cannilla, C., Arena, F., & Frusteri, F. (2014). The changing nature of the active site of Cu-Zn-Zr catalysts for the CO2 hydrogenation reaction to methanol. *Applied catalysis*, 152-161.

Brahic, C. (2007). *The impacts of rising global temperatures*. Retrieved from New Scientist: https://www.newscientist.com/article/dn11562-climate-change-is-here-now-says-major-report/

Brunauer, S., Deming, L. S., Deming, W. E., & Teller, E. (1940). On a Theory of the van der Waals Adsorption of Gases. *Journal of the American Chemical Society*, 1723-1732.

Brunauer, S., Emmett, P. H., & Teller, E. (1938). Adsorption of Gases in Multimolecular Layers. *Journal of the American Chemical Society*, 309-319.

Carbon recycling international. (2022). *THE SHUNLI CO2 -TO-METHANOL PLANT: COMMERCIAL SCALE PRODUCTION IN CHINA*. Retrieved from Carbon recycling international: https://www.carbonrecycling.is/projects-shunli

Catlow, C., French, S., Sokol, A., & Thomas, J. (2005). Computational approaches to the determination of active site structures and reaction mechanisms in heterogeneous catalysts. *Philosophical transactions of the Royal Society of London. Series A: Mathematical, physical, and engineering sciences*, 913-936.

Chorkendorff, I., Rasmussen, P., & Kazuta, M. (1994). Synthesis of methanol from a mixture of H2 and CO2 on Cu(100). *Surface science*, 267-280.

Chou, C.-Y. (2019). *Catalytic CO2 Hydrogenation to Co and Methanol.* ProQuest Dissertations Publishing.

Chou, C.-Y., & Lobo, R. F. (2019). Direct conversion of CO2 into methanol over promoted indium oxide-based catalysts. *Applied catalysis*, 117144.

Deerattrakul, V., Dittanet, P., Sawangphruk, M., & Kongkachuichay, P. (2016). CO2 hydrogenation to methanol using Cu-Zn catalyst supported on reduced graphene oxide nanosheets. *Journal of CO2 utilization*, 104-113.

Deerattrakul, V., Limphirat, W., & Kongkachuichay, P. (2017). Influence of reduction time of catalyst on methanol synthesis via CO2 hydrogenation using Cu–Zn/N-rGO investigated by in situ XANES. *Journal of the Taiwan Institute of Chemical Engineers*, 495-502.

Deerattrakul, V., Puengampholsrisook, P., Limphirat, W., & Kongkachuichay, P. (2018). Characterization of supported Cu-Zn/graphene aerogel catalyst for direct CO2 hydrogenation to methanol: Effect of hydrothermal temperature on graphene aerogel synthesis. *Catalysis today*, 154-163.

Deerattrakul, V., Yigit, N., Rupprechter, G., & Kongkachuichay, P. (2019). The roles of nitrogen species on graphene aerogel supported Cu-Zn as efficient catalysts for CO2 hydrogenation to methanol. *Applied catalysis. A, General*, 46-52.

Denise, B., Cherifi, O., Bettahar, M., & Sneeden, R. (1989). Supported Copper Catalysts Prepared from Copper(II) Formate. Hydrogenation of Carbon Dioxide Containing Feedstocks. *Applied catalysis*, 365-372.

Din, I. U., Shaharun, M. S., Alotaibi, M. A., Alharthi, A. I., & Naeem, A. (2019). Recent developments on heterogeneous catalytic CO2 reduction to methanol . *Journal of CO2 utilization*, 20-33.

Din, I. U., Shaharun, M. S., Naeem, A., Tasleem, S., & Johan, M. R. (2017). Carbon nanofiber-based copper/zirconia catalyst for hydrogenation of CO2 to methanol. *Journal of CO2 utilization*, 145-155.

Dong, X., Zhang, H.-B., Lin, G.-D., Yuan, Y.-Z., & Tsai, K. (2002). Highly active EAG-promoted Cu-ZnO-Al2O3 catalyst for methanol synthesis from H2/CO/CO2. *Catalysis letters*, 237-246.

EPA. (2023). *Greenhouse Gas Emissions*. Retrieved from EPA: https://www.epa.gov/ghgemissions/global-greenhouse-gas-emissions-data

Erdogan Alper, O. Y. (2017). CO2 utilization: Developments in conversion processes. *Petroleum*, 109-126.

Fan. (2021). *Catalytic Carbon Dioxide Hydrogenation to Methanol/Dimethyl Ether over Copper-Based Catalysts.* ProQuest Dissertations Publishing.

Fan, Y. J., & Wu, S. F. (2016). A graphene-supported copper-based catalyst for the hydrogenation of carbon dioxide to form methanol. *Journal of CO2 utilization*, 150-156.

French, S., Sokol, A., Bromley, S., Catlow, C., & Sherwood, P. (2003). Identification and characterization of active sites and their catalytic processes - The Cu/ZnO methanol catalyst. *Topics in catalysis*, 161-172.

Fujitani, T., Nakamura, I., Ueno, S., Uchijima, T., & Nakamura, J. (1997). Methanol synthesis by hydrogenation of CO2 over a Zn-deposited Cu(111) : formate intermediate. *Applied surface science*, 583-586.

Gaikwad, R. (2018). *Carbon Dioxide To Methanol: Stoichiometric Catalytic Hydrogenation Under High Pressure Conditions.* Universitat Rovira i Virgili.

Gao, J. (2021). *A study of carbon dioxide catalytic activation for its conversion to value-added products.* Saskatoon: University of Saskatchewan.

Gao, P., Li, F., Zhao, N., Xiao, F., Wei, W., Zhong, L., & Sun, Y. (2013). Influence of modifier (Mn, La, Ce, Zr and Y) on the performance of Cu/Zn/Al catalysts via hydrotalcite-like precursors for CO2 hydrogenation to methanol. *Applied Catalysis*, 442–452.

Gesmanee, S., & Koo-Amornpattana, W. (2017). Catalytic hydrogenation of CO2 for methanol production in fixed-bed reactor using Cu-Zn supported on gamma-Al2O3. *Energy Procedia*, 739-744.

Global CO2 levels. (2023). Retrieved from N2olevels: https://www.n2olevels.org

Goeppert, A., Czaun, M., Jones, J.-P., Surya Prakash, G. K., & Olah, G. A. (2014). Recycling of carbon dioxide to methanol and derived products - closing the loop . *Chemical Society reviews*, 7995-848.

Graciani, J., Mudiyanselage, K., Xu, F., Baber, A. E., Evans, J., Senanayake, S. D., . . . Rodriguez, J. A. (2014). Highly active copper-ceria and copper-ceria-titania catalysts for methanol synthesis from CO2. *Science (American Association for the Advancement of Science)*, 546-550.

Großmann, D. (2013). *Methanol Synthesis over Cu/ZnO aggregates encapsulated in carbon nanotubes and mesoporous silica.* Ruhr-Universität Bochum.

Großmanna, D., Dreierb, A., Lehmannb, C., & Grünerta, W. (2015). Methanol synthesis over Cu–ZnO aggregates supported on carbonnanotubes. *Applied Catalysis A: General*.

Guo, X., Mao, D., Lu, G., Wang, S., & Wu, G. (2010). Glycine-nitrate combustion synthesis of CuO-ZnO-ZrO2 catalysts for methanol synthesis from CO2 hydrogenation. *Journal of catalysis*, 178-185.

Hobson, C. a. (2018). *Renewable Methanol Report.* Methanol Institute.

IEA . (2022, OCt 26). *Venture Capital investments in CCU start-ups, 2015-2021*. Retrieved from IEA: https://www.iea.org/data-and-statistics/charts/venture-capital-investments-in-ccu-start-ups-2015-2021

IEA. (2023, March). *CO2 Emissions in 2022*. Retrieved from IEA: https://www.iea.org/reports/co2-emissions-in-2022

Inui, T., Kitagawa, K., Takeguchi, T., Hagiwara, T., & Makino, Y. (1993). Hydrogenation of carbon dioxide to C1-C7 hydrocarbons via methanol on composite catalysts. *Applied catalysis. A*, 31-44.

Jabbour, K. (2020). *Combined and dry reforming of methane on new Ni0/diatoms and mesoporous Ni0/alumina catalysts.* Université Pierre et Marie Curie.

Jung, K. T., & Bell, A. T. (2002). Effects of zirconia phase on the synthesis of methanol over zirconia-supported copper. *Catalysis letters*, 63-68.

Kühl, S., Tarasov, A., Zander, S., Kasatkin, I., & Behrens, M. (2014). Cu-Based Catalyst Resulting from a Cu,Zn,Al Hydrotalcite-Like Compound: A Microstructural, Thermoanalytical, and In Situ XAS Study. *Chemistry : a European journal*, 3782-3792.

Kanoun, N., Astier, M., & Pajonk, G. (1992). Catalytic properties of new Cu based catalysts containing Zr and/or V for methanol synthesis from a carbon dioxide and hydrogen mixture. *Catalysis letters*, 231-235.

Karelovic, A., Bargibant, A., Fernández, C., & Ruiz, P. (2012). Effect of the structural and morphological properties of Cu/ZnO catalysts prepared by citrate method on their activity toward methanol synthesis from CO2 and H2 under mild reaction conditions. *Catalysis today*, 109-118.

Kasatkin, I., Kurr, P., Kniep, B., Trunschke, A., & Schlögl, R. (2007). Role of Lattice Strain and Defects in Copper Particles on the Activity of Cu/ZnO/Al_2O_3 Catalysts for Methanol Synthesis. *Angewandte Chemie (International ed.*, 7324-7327.

Kattel, S., Ramírez, P. J., Chen, J. G., Rodriguez, J. A., & Liu, P. (2017). Active sites for CO_2 hydrogenation to methanol on Cu/ZnO catalysts . *Science (American Association for the Advancement of Science)*, 1296-1299.

Kattel, S., Yan, B., Yang, Y., Chen, J. G., & Liu, P. (2016). Optimizing Binding Energies of Key Intermediates for CO2 Hydrogenation to Methanol over Oxide-Supported Copper. *Journal of the American Chemical Society*, 12440-12450.

Kiehl, J. T., & Trenberth, K. E. (1997). Bulletin of the American Meteorological Society. *Earth's Annual Global Mean Energy Budget*, 197-208.

Kruk, M., & Jaroniec, M. (2001). Gas Adsorption Characterization of Ordered Organic−Inorganic Nanocomposite Materials. *Chemistry of materials*, 3169-3183.

Kuld, S., Thorhauge, M., Falsig, H., Elkjær, C. F., Helveg, S., Chorkendorff, I., & Sehested, J. (2016). Quantifying the promotion of Cu catalysts by ZnO for methanol synthesis . *Science (American Association for the Advancement of Science)*, 969-974.

Kunkes, E. L., Studt, F., Abild-Pedersen, F., Schlögl, R., & Behrens, M. (2015). Hydrogenation of CO2 to methanol and CO on Cu/ZnO/Al2O3: Is there a common intermediate or not? *Journal of catalysis*, 43-48.

Larmier, K., Liao, W.-C., Tada, S., Lam, E., Verel, R., Bansode, A., . . . Copéret, C. (2017). CO2-to-Methanol Hydrogenation on Zirconia-Supported Copper Nanoparticles: Reaction Intermediates and the Role of the Metal–Support Interface. *Angewandte Chemie (International ed.)*, 2318-2323.

Lawrie, L. (2011). Ammonia and Methanol Synthesis. *Springer US*, 397-437.

Lee, J. S., Moon, K. I., Lee, S. H., Lee, S. Y., & Kim, Y. G. (1995). Modified Cu/ZnO/Al2O3 catalysts for methanol synthesis from CO2/H2 and CO/H2. *Catalysis Letters*, 93–99.

Li, K., & Chen, J. G. (2019). CO2 Hydrogenation to Methanol over ZrO2-Containing Catalysts: Insights into ZrO2 Induced Synergy. *ACS catalysis*, 7840-7861.

Li, L., Mao, D., Yu, J., & Guo, X. (2015). Highly selective hydrogenation of CO.sub.2 to methanol over CuO-ZnO-ZrO.sub.2 catalysts prepared by a surfactant-assisted co-precipitation method. *Journal of power sources*, 394.

Liang, X.-L., Dong, X., Lin, G.-D., & Zhang, H.-B. (2009). Carbon nanotube-supported Pd–ZnO catalyst for hydrogenation of CO2 to methanol. *Applied Catalysis. B, Environmental*, 315–322.

Liao, F., Huang, Y., Ge, J., Zheng, W., Tedsree, K., Collier, P., . . . Tsang, S. C. (2011). Morphology-Dependent Interactions of ZnO with Cu Nanoparticles at the Materials' Interface in Selective Hydrogenation of CO2 to CH3OH. *Angewandte Chemie*, 2210-2213.

Liu, S.-H., Wang, H. P., Wang, H.-C., & Yang, Y. (2005). In situ EXAFS studies of copper on ZrO2 during catalytic hydrogenation of CO2 . *Journal of electron spectroscopy and related phenomena*, 373-376.

Liu, Z.-J., Tang, X.-J., Xu, S., & Wang, X.-L. (2014). Synthesis and catalytic performance of graphene modified CuO-ZnO-Al2O3 for CO2 hydrogenation to methanol. *Journal of nanomaterials*.

Lowell, S., Shields, J. E., Thomas, M. A., & Thommes, M. (2004). *Characterization of Porous Solids and Powders: Surface Area, Pore Size and Density.* Springer Dordrecht.

Ma, Q., Geng, M., Zhang, J., Zhang, X., & Zhao, T.-S. (2018). Enhanced Catalytic Performance for CO2 Hydrogenation to Methanol over N-doped Graphene Incorporated Cu-ZnO-Al2O3 Catalysts. *ChemistrySelect (Weinheim)*, 78-83.

Martin, O., Martín, A. J., Mondelli, C., Mitchell, S., Segawa, T. F., Hauert, R., . . . Pérez-Ramírez, J. (2016). Indium Oxide as a Superior Catalyst for Methanol Synthesis by CO2 Hydrogenation. *Angewandte Chemie*, 6261-6265.

Martínez-Suárez, L., Frenzel, J., & Marx, D. (2014). Cu/ZnO nanocatalysts in response to environmental conditions: Surface morphology, electronic structure, redox state and CO2 activation. *Physical chemistry chemical physics*, 26119-26136.

Martínez-Suárez, L., Frenzel, J., Marx, D., & Meyer, B. (2013). Tuning the reactivity of a Cu/ZnO nanocatalyst via gas phase pressure. *Physical review letters*, 086108-086108.

Martínez-Suárez, L., Siemer, N., Frenzel, J., & Marx, D. (2015). Reaction Network of Methanol Synthesis over Cu/ZnO Nanocatalysts . *ACS catalysis*, 4201-4218.

Methanol Institute. (2016). *Global Market Trajectory & Analytics.* Retrieved from Methanol: https://www.methanol.org/wp-content/uploads/2016/07/6-Combined-Side-Deck-GFBC-1.pdf

Methanol Market. (2021, Dec). Retrieved from Market and Methanol: https://www.marketsandmarkets.com/Market-Reports/methanol-market-425.html?gclid=Cj0KCQjwr82iBhCuARIsAO0EAZzc8jOwqVC7ufo5WIfNpqpnU7bXBXscQ7IH0r_an4u_r9dMdMkAJUQaAg1UEALw_wcB

Mihet, M., Dan, M., & Lazar, M. (2020). CO2 Hydrogenation Catalyzed by Graphene-Based Materials. *Molecules (Basel, Switzerland)*, 3367–.

Minett, D. (2013). *Carbon Dioxide conversion to hydrocarbons with reactivated iron-carbon nanotube catalysts.* University of Bath.

Morikawa, Y., Iwata, K., & Terakura, K. (2001). Theoretical study of hydrogenation process of formate on clean and Zn deposited Cu(1 1 1) surfaces. *Applied surface science*, 11-15.

Murkin, C., & Brightling, J. (2016). Eighty Years of Steam Reforming . *Johnson Matthey Technology Review*, 263-269.

Nakamura, J., Nakamura, I., Uchijima, T., Kanai, Y., Watanabe, T., Saito, M., & Fujitani, T. (1996). A Surface Science Investigation of Methanol Synthesis over a Zn-Deposited Polycrystalline Cu Surface. *Journal of catalysis*, 65-75.

Nam, S.-S., Kim, H., Kishan, G., Choi, M.-J., & Lee, K.-W. (1999). Catalytic conversion of carbon dioxide into hydrocarbons over iron supported on alkali ion-exchanged Y-zeolite catalysts. *Applied catalysis. A, General*, 155-163.

Nieto, A. (2021). *Carbon nanotubes : reinforced metal matrix composites (Second edition.).* CRC Press.

Nitta, Y., Suwata, O., Ikeda, Y., Okamoto, Y., & Imanaka, T. (1994). Copper-zirconia catalysts for methanol synthesis from carbon dioxide: Effect of ZnO addition to Cu-ZrO2 catalysts. *Catalysis letters*, 345-354.

Olah, G. A. (2005). Beyond Oil and Gas: The Methanol Economy. *Angewandte Chemie (International ed.)*, 2636-2639.

Pan, X., & Bao, X. (2008). Reactions over catalysts confined in carbon nanotubes . *Chemical Communications*, 6271-6281.

Petrucci, R. H. (2007). *General Chemistry : Principles and Modern Applications. 9th ed.* Upper Saddle River, N.J: Pearson/Prentice Hall.

Polierer, S., Jelic, J., Pitter, S., & Studt, F. (2019). On the Reactivity of the Cu/ZrO2 System for the Hydrogenation of CO2 to Methanol: A Density Functional Theory Study. *Journal of physical chemistry*, 26904-26911.

Rase, H. F. (2000). *Handbook of commercial catalysts : heterogeneous catalysts .* Boca Raton, Fla. : CRC Press.

Rasmussen, P., Holmblad, P., Askgaard, T., Ovesen, C., Stoltze, P., Nørskov, J., & Chorkendorff, I. (1994). Methanol synthesis on Cu(100) from a binary gas mixture of CO2 and H2. *Catalysis letters*, 373-381.

Reichenbach, T., Mondal, K., Jäger, M., Vent-Schmidt, T., Himmel, D., Dybbert, V., . . . Moseler, M. (2018). Ab initio study of CO2 hydrogenation mechanisms on inverse ZnO/Cu catalysts. *Journal of catalysis*, 168-174.

Ribeiro, B., Botelho, E. C., Costa, M. L., & Bandeira, C. F. (2017). Carbon nanotube buckypaper reinforced polymer composites: A review. *Polímeros, Ciência e Tecnologia*, Vol.27 (3), p.247-255.

Rosca, I. D., Watari, F., Uo, M., & Akasaka, T. (n.d.). Oxidation of multiwalled carbon nanotubes by nitric acid. *Carbon (New York)*, 3124–3131.

S. Arrhenius. (1896). *Philosophical Magazine and Journal of Science Series 5*, 237-276.

Samson, K., Śliwa, M., Socha, R. P., Góra-Marek, K., Mucha, D., Rutkowska-Zbik, D., . . . Słoczyński, J. (2014). Influence of ZrO2 Structure and Copper Electronic State on Activity of Cu/ZrO2 Catalysts in Methanol Synthesis from CO2. *ACS catalysis*, 3730-3741.

San, X., Gong, X., Hu, Y., Hu, Y., Wang, G., Qi, J., . . . Jin, Q. (2021). Highly Dispersed Cu/Graphene Nanocatalyst Guided by MOF Structure: Application to Methanol Synthesis from CO2 Hydrogenation. *ChemistrySelect (Weinheim)*, 6115-6118.

Schild, C., Wokaun, A., & Baiker, A. (1991). On the hydrogenation of CO and CO2 over copper/zirconia and palladium/zirconia catalysts. *Fresenius' Journal of Analytical Chemistry,*, 395-401.

Senanayake, S. D., Ramirez, P. J., Waluyo, I., Kundu, S., Mudiyanselage, K., Liu, Z., . . . Rodriguez, J. A. (2016). Hydrogenation of CO2 to methanol on CeOx/Cu(111) and ZnO/Cu(111) catalysts: Role of the metal-oxide interface and importance of Ce3+ sites. *Journal of physical chemistry*.

Sheldon, D. (2017). Methanol Production – A Technical History. *JOHNSON MATTHEY TECHNOLOGY REVIEW*, 172–182.

Sing, K. S. (1985). Reporting physisorption data for gas/solid systems with special reference to the determination of surface area and porosity (Recommendations 1984). *Pure and applied chemistry*, 603-619.

Skoog, D. A., Holler, F. J., & Crouch, S. R. (2018). *Principles of instrumental analysis. Seventh edition.* Boston, Massachusetts: Cengage Learning.

Solid-state interactions, adsorption sites and functionality of Cu-ZnO/ZrO2 catalysts in the CO2 hydrogenation to CH3OH. (2008). *Arena, Francesco ; Italiano, Giuseppe ; Barbera, Katia ; Bordiga, Silvia ; Bonura, Giuseppe ; Spadaro, Lorenzo ; Frusteri, Francesco;*, 16-23.

Solomon, E. I., Jones, P. M., & May, J. A. (1993). Electronic structures of active sites on metal oxide surfaces: definition of the copper-zinc oxide methanol synthesis catalyst by photoelectron spectroscopy. *Chem. Rev*, 2623–2644.

Stangeland, K. (2021). *Catalytic conversion of CO2 to methanol via CO2 hydrogenation : An investigation of metal oxide promoted catalysts.* Stavanger: University of Stavanger.

Studt, F., Behrens, M., Kunkes, E. L., Thomas, N., Zander, S., Tarasov, A., . . . Schlögl, R. (2015). The Mechanism of CO and CO2 Hydrogenation to Methanol over Cu-Based Catalysts. *ChemCatChem*, 1105-1111.

Sun, Y., Chen, L., Bao, Y., Wang, G., Zhang, Y., Fu, M., . . . Ye, D. (2018). Roles of nitrogen species on nitrogen-doped EAGs supported Cu-ZrO2 system for carbon dioxide hydrogenation to methanol. *Catalysis today*, 212-223.

Tada, S., Kayamori, S., Honma, T., Kamei, H., Nariyuki, A., Kon, K., . . . Satokawa, S. (2018). Design of Interfacial Sites between Cu and Amorphous ZrO2 Dedicated to CO2-to-Methanol Hydrogenation. *ACS catalysis*, 7809-7819.

Tao, H., Li, Y., Cai, X., Zhou, H., Li, Y., Lin, W., . . . Zhang, Y. (2019). What Is the Best Size of Subnanometer Copper Clusters for CO2 Conversion to Methanol at Cu/TiO2 Interfaces? A Density Functional Theory Study. *Journal of physical chemistry*, 24118-24132.

Tsang, S. C., Chen, Y. K., Harris, P. J., & Green, M. L. (1994). A simple chemical method of opening and filling carbon nanotubes. *Nature (London)*, 159-162.

Ud Din, I., Shaharun, M. S., Subbarao, D., & Naeem, A. (2015). Synthesis, characterization and activity pattern of carbon nanofibers based copper/zirconia catalysts for carbon dioxide hydrogenation to methanol: Influence of calcination temperature. *Journal of power sources*, 619-628.

UNFCCC. (2015). Decision 1/CP.21: Adoption of the Paris Agreement. Paris Climate Change Conference. Paris, France.

Van Der Grift, C., Wielers, A., Jogh, B., Van Beunum, J., De Boer, M., Versluijs-Helder, M., & Geus, J. (1991). Effect of the reduction treatment on the structure and reactivity of silica-supported copper particles. *Journal of catalysis*, 178-189.

Verhelst, S., Turner, J. W., Sileghem, L., & Vancoillie, J. (2019). Methanol as a fuel for internal combustion engines . *Progress in energy and combustion science*, 43-88.

Wang, C., Fang, Y., Liang, G., Lv, X., Duan, H., Li, Y., . . . Long, M. (2021). Mechanistic study of Cu-Ni bimetallic catalysts supported by graphene derivatives for hydrogenation of CO2 to methanol. *Journal of CO2 utilization*, 101542.

Wang, C., Guo, S., Pan, X., Chen, W., & Bao, X. (2008). Tailored cutting of carbon nanotubes and controlled dispersion of metal nanoparticles inside their channels. *Journal of materials chemistry*, 5782-5786.

Wang, G., Chen, L., Sun, Y., Wu, J., Fu, M., & Ye, D. (2015). Carbon dioxide hydrogenation to methanol over Cu/ZrO2/EAGs: Effect of carbon surface chemistry. *RSC advances*, 45320-45330.

Wang, W., Wang, S., Ma, X., & Gong, J. (2011). Recent advances in catalytic hydrogenation of carbon dioxide. *Chemical Society Reviews*, 3703–3727.

Wang, Y., Kattel, S., Gao, W., Li, K., Liu, P., Chen, J. G., & Wang, H. (2019). Exploring the ternary interactions in Cu–ZnO–ZrO2 catalysts for efficient CO2 hydrogenation to methanol. *Nature communications*, 1166-1166.

Waugh, K. C. (1992). Methanol synthesis: Fuel extenders and additives. *Catalysis today*, 51-75.

Weigel, J., Koeppel, R. A., Baiker, A., & Wokaun, A. (1996). Surface Species in CO and CO2 Hydrogenation over Copper/Zirconia: On the Methanol Synthesis Mechanism. *Langmuir*, 5319-5329.

Witoon, T., Numpilai, T., Phongamwong, T., Donphai, W., Boonyuen, C., Warakulwit, C., . . . Limtrakul, J. (2018). Enhanced activity, selectivity and stability of a CuO-ZnO-ZrO2 catalyst by adding graphene oxide for CO2 hydrogenation to methanol. *Chemical engineering journal (Lausanne, Switzerland : 1996)*, 1781-1791.

Yang, B., Liu, C., Halder, A., Tyo, E. C., Martinson, A. B., Seifert, S., . . . Vajda, S. (2017). Copper Cluster Size Effect in Methanol Synthesis from CO2 . *Journal of physical chemistry*, 10406-10412.

Yang, C., Ma, Z., Zhao, N., Wei, W., Hu, T., & Sun, Y. (2006). Methanol synthesis from CO.sub.2-rich syngas over a ZrO.sub.2 doped CuZnO catalyst. *Catalysis today*, 222.

Yang, Y., Mims, C., Mei, D., Peden, C., & Campbell, C. (2013). Mechanistic studies of methanol synthesis over Cu from CO/CO2/H2/H2O mixtures: The source of C in methanol and the role of water. *Journal of catalysis*, 10-17.

Yu, M.-F., Lourie, O., Dyer, M. J., Moloni, K., Kelly, T. F., & Ruoff, R. S. (2000). Strength and Breaking Mechanism of Multiwalled Carbon Nanotubes under Tensile Load. *Science (American Association for the Advancement of Science)*, 637–640.

Yu, X., Huo, Y., Yang, J., Chang, S., Ma, Y., & Huang, W. (2013). Reduced graphene oxide supported Au nanoparticles as an efficient catalyst for aerobic oxidation of benzyl alcohol. *Applied Surface Science*, 450–455.

Zabilskiy, M., Sushkevich, V. L., Palagin, D., Newton, M. A., Krumeich, F., & van Bokhoven, J. A. (2020). The unique interplay between copper and zinc during catalytic carbon dioxide hydrogenation to methanol. *Nature communications*, 2409-2409.

Zapantis, A., Al Amer, N., Havercroft, I., Ivory-Moore, R., Steyn, M., Yang, X., . . . Minervini, J. (2022). *GLOBAL STATUS OF CCS 2022.* Global CCS Institute.

Zhang, Q., Zuo, Y.-Z., Han, M.-H., Wang, J.-F., Jin, Y., & Wei, F. (2010). Long carbon nanotubes intercrossed Cu/Zn/Al/Zr catalyst for CO/CO2 hydrogenation to methanol/dimethyl ether. *Catalysis today*, 55-60.

Zhang, Q., Zuo, Y.-Z., Han, M.-H., Wang, J.-F., Jin, Y., & Wei, F. (2010). Long carbon nanotubes intercrossed Cu/Zn/Al/Zr catalyst for CO/CO2 hydrogenation to methanol/dimethyl ether. *Catalysis Today*, 55–60.

Zheng, H., Narkhede, N., Han, L., Zhang, H., & Li, Z. (2020). Methanol synthesis from CO2: a DFT investigation on Zn-promoted Cu catalyst. *Research on chemical intermediates*, 1749-1769.

Appendix A - Reactor Parts

Fundamental reactor parts, the model and the brand of the purchase are shown in Appendix Table A.

Appendix Table A: List of Fundamental Reactor Parts, Brands, and Models

Part	Quantity	Brand	Model
Flexible braided hose	3	Swagelok	SS-FM4TA4TA4-24
Ball Valve	3	Swagelok	SS-43GVS4
1/4 " Stainless steel tubing	1	Swagelok	SS-T4-S-035-6ME
Mass flow controller	3	Bronkhorst	EL-FLOW PRESTIGE FG-201CV
Check valve	3	Swagelok	SS-4C-1/3
Pressure transducer	1	Swagelok	PTI- S- AG40- X X AO
Reactor	1	Swagelok	SS-T4-S-035-6ME
Filter	1	Swagelok	SS-4F-05
Back Pressure regulator	1	Bronkhorst	EL-PRESS P-702CV (P1-CONTROL)

Appendix Table A shows the purchased connection required to connect the parts.

Appendix Table B: List of required connections for reactor parts.

Part			Connection		
Part	Quantity	Part's Outlet	Brand	Model	Required quantity
Double stage regulator	3	3/8 female	Swagelok	SS-400-1-6RT	1
Ball valve	3	1/4" Swagelok Tube Fitting	NA	NA	NA
EL-Flow	3	1/4" BSPP female thread	Swagelok	SS-400-1-4RS	6
Check Valve	3	1/4" Swagelok Tube Fitting	NA	NA	NA
Merge	1	none	Swagelok	SS-400-4	1
Pressure Transducer	1	1/4 in. male NPT	Swagelok	Female Tee/ SS-400-3-4TTF	1
Reactor	1	1/4" Swagelok Tube Fitting	Swagelok	Union/ SS-4FK0-6	2
Filter	1	1/4" Swagelok Tube Fitting	NA	NA	NA
El-Press	1	1/4" BSPP female thread	Swagelok	SS-400-1-4RS	2

Appendix B - N_2O Chemisorption

Cu surface area, Cu dispersion, and Cu crystallite size were obtained by N_2O-chemisorption measurements using Micromeritics Autochem II 2920. Before measurements, the samples were degassed at 250 °C in a pure Ar flow and further reduced at the same temperature in a 10 vol.% of H_2 in Ar flow for 2 hours, then cooled down to 50 °C with an Ar flow. After that, a mixture of 1 vol.% N_2O in He gas was used to conduct chemisorption process. The Cu surface area and Cu dispersion values were calculated assuming a Cu: N_2O = 2:1 stoichiometry.

The Micromeritics Autochem II ASAP 2920 instrument assessed the exposed surface area of copper. Before initiating the N_2O adsorption process, the sample underwent a series of steps: it was initially heated to 200 °C under argon flow for 0.5 hours, then reduced in a 5% hydrogen (H_2) in Ar atmosphere at 350 °C for 2 hours, and subsequently purged with Ar until the temperature dropped to 50 °C. The decomposition of N_2O adsorbed on the sample was carried out in a mixture containing 1% N_2O in Ar at 50 °C for 1 hour, as described by (Van Der Grift et al. 1991). The sample tube was purged with Ar for 1 hour to eliminate any physically adsorbed N_2O. To determine N_2O consumption, an H2-TPR experiment was performed, ranging from 50 to 400 °C at a heating rate of 10 °C per minute in a mixture of 7% H_2 in Ar. The Cu surface area (SA_{Cu}) was estimated using the following equation based on the H_2 consumption.

$$SA_{Cu}(m^2.g_{cat}^{-1}) = \frac{Y \times SF \times N_A}{C_M \times W_{cat}}$$

where Y is the moles of H_2 consumed in the TPR following N_2O chemisorption, SF is the stoichiometric factor (2), N_A is Avogadro's number (6.022 × 1023 mol^{-1}), C_M is the number of surface Cu atoms per unit surface area (1.47 × 1019 atoms·m^{-2}), and W_{cat} is the amount of catalyst (g).